



The surface and bulk oxidation of zirconium
by Brian Paul Thiesen

A thesis submitted in partial fulfillment of the requirements for the degree of Master of Science in
Chemical Engineering
Montana State University
© Copyright by Brian Paul Thiesen (1988)

Abstract:

The oxidation of zirconium at high temperatures involves both the formation of a surface oxide, and absorption of oxygen into the bulk Zr. The hcp lattice of Zr is reported to absorb up to 29.8 at. % oxygen, which occupies the interstitial sites. The simultaneous surface oxidation and diffusion of oxygen into the bulk Zr were observed at temperatures of 1073, 1173 and 1243 K. Experimental results were compared to predicted results from a model developed here to evaluate values of the oxidation kinetic parameters. Samples of Zr, 0.025 cm thick, were saturated with oxygen by soaking surface-oxidized samples in an argon atmosphere at 1243 K. The initial surface oxidation properties of saturated Zr were compared to pure Zr by AES-analysis.

The model of the oxidation process assumes that diffusion of O_2 - through the oxide layer is rate limiting. The oxide growth at the oxide Zr interface is described by a mass balance. The principle parameter in the model is the product, D/δ , the diffusion coefficient of oxygen in ZrO_2 and the oxygen concentration difference across the oxide. The model was calibrated by two completely separate methods. The first compared model predicted curves of mass vs. time to those produced experimentally. The second method compared predicted oxide thicknesses at specific times and temperatures with those observed experimentally. A value for δ from the literature was assumed. Then D , as a function of temperature was determined for both experimental methods. From the mass gain curve fitting method the diffusion coefficient, $D = 1.6 \times 10^{-5} \exp(-20700/RT)$ was found. From the oxide thickness comparison the diffusion coefficient, $D = 2.0 \times 10^{-2} \exp(-34300/RT)$ was found. It is concluded that the primary oxygen diffusion path is along grain boundaries, and that D is a function of extent of oxidation due to changing oxide crystal size during oxidation.

Saturated and pure Zr samples were exposed to successive exposures of O_2 at room temperature, interrupted by sequential AES analysis. Results of the AES study indicate that Zr:Oss surface oxidation is essentially the same as that of pure Zr. The oxygen concentration of sputter-cleaned Zr:Oss was estimated to be 28.8 at. % oxygen by quantitative AES analysis.

THE SURFACE AND BULK OXIDATION OF ZIRCONIUM

by

Brian Paul Thiesen

A thesis submitted in partial fulfillment
of the requirements for the degree

of

Master of Science

in

Chemical Engineering

MONTANA STATE UNIVERSITY
Bozeman, Montana

March 1988

N378
T3475

APPROVAL

of a thesis submitted by

Brian Paul Thiesen

This thesis has been read by each member of the thesis committee and has been found to be satisfactory regarding content, English usage, format, citations, bibliographic style, and consistency, and is ready for submission to the College of Graduate Studies.

April 6, 88
Date

Max C. Deiber
Chairperson, Graduate Committee

Approved for the Major Department

April 7, 88
Date

John T. Sears
Head, Major Department

Approved for the College of Graduate Studies

4-14-88
Date

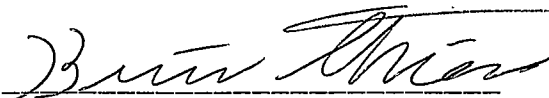
Ms Malone
Graduate Dean

STATEMENT OF PERMISSION TO USE

In presenting this thesis in partial fulfillment of the requirements for a master's degree at Montana State University, I agree that the Library shall make it available to borrowers under rules of the Library. Brief quotations from this thesis are allowable without special permission, provided that accurate acknowledgment of source is made.

Permission for extensive quotation from or reproduction of this thesis may be granted by my major professor, or in his absence, by the Dean of Libraries when, in the opinion of either, the proposed use of the material is for scholarly purposes. Any copying or use of the material in this thesis for financial gain shall not be allowed without my written permission.

Signature



Date

4-13-88

ACKNOWLEDGMENTS

The author wishes to thank the faculty and staff of the Chemical Engineering Department at Montana State University for their guidance and assistance.

Special thanks to Dr. M. Deibert for his advice and support throughout the course of this research and thesis preparation.

The author also wishes to thank Dr. Frank P. McCandless and Dr. Robert L. Nickelson for the use of their equipment and assistance.

TABLE OF CONTENTS

	Page
APPROVAL.....	ii
STATEMENT OF PERMISSION TO USE.....	iii
ACKNOWLEDGMENTS.....	iv
TABLE OF CONTENTS.....	v
LIST OF TABLES.....	viii
LIST OF FIGURES.....	ix
ABSTRACT.....	xii
INTRODUCTION.....	1
Background.....	1
Related Research.....	3
General Characteristics.....	4
Effect of Oxygen Pressure on the Oxidation of Zr.....	8
Effect of the Oxidizing Agent.....	8
Diffusion Characteristics.....	9
Surface Science.....	11
RESEARCH OBJECTIVES.....	13
MODEL DEVELOPMENT.....	14
Mechanisms During Surface Oxidation of Zr.....	14
Ionic Transport in the Oxide.....	16
Electron Transport in the Oxide.....	19
Migration of Oxygen Through the Oxide.....	20
Development of a Mathematical Model.....	20
Adsorption.....	21
Mass Flux Across the Oxide.....	21
Diffusion of Oxygen into the Bulk Zr.....	22
Interface.....	23
Boundary Conditions.....	26

TABLE OF CONTENTS-Continued

	Page
EXPERIMENTAL EQUIPMENT.....	32
Reactor for Oxidation and Saturation of Zr.....	32
Surface Spectroscopy Methods.....	34
Scanning Electron Microscopy.....	34
Auger Electron Spectroscopy.....	35
EXPERIMENTAL PROCEDURES.....	37
Oxidation and Saturation Procedures.....	37
Sample Preparation.....	37
Experimental Equipment and Procedure.....	38
Determination of Time to Saturate Samples.....	40
AES Analysis Procedure.....	41
SEM Analysis Procedure.....	43
RESULTS AND DISCUSSION.....	45
Analysis of Saturated Zirconium.....	45
AES Spectra Analysis by Seah Method.....	46
Depth Profile.....	49
Initial Oxidation at Room Temperature.....	51
Diffusion Coefficient Determination.....	54
Model Application.....	55
Isothermal Model Correlations from	
Curve Fitting Method.....	58
Evaluation of $D_o \delta C_o$ from Curve Fitting.....	60
Experimental Error Involved with Curve Fitting..	64
Isothermal Model Correlations with	
Oxide Thickness Measurements.....	67
Evaluation of $D_o \delta C_o$ from Experimental	
Oxide Thicknesses.....	69
Experimental Error Involved with	
Oxide Thicknesses.....	69
Determination of D_o as a Function of Temperature..	71
Deviations Between Experimental and	
Published Values of D_o	74
Changing Characteristics of the Oxide.....	76
Effect of Warm-Up and Cool-Down.....	77
CONCLUSIONS.....	83
RECOMMENDATIONS FOR FUTURE RESEARCH.....	84
REFERENCES CITED.....	85

TABLE OF CONTENTS-Continued

	Page
APPENDIX.....	89
Computer Program: Temperature control in the reactor.....	90
Computer Program: Isothermal Model I.....	91
Computer Program: Non-isothermal Model II.....	95
Computer Program: Model III, Diffusion model to determine the time to reach 99.99% saturation at the midplane.	99

LIST OF TABLES

Table	Page
1. Variables used in the model.....	28
2. Exposure times and pressures utilized in Surface oxidation study.....	43
3. Predicted times to reach 99.99% saturation at midplane and actual time of run.....	45
4. AES primary peak intensities for pure and Zr:Oss.....	54
5. Oxidation conditions of each Zr sample.....	57
6. Percent of total time sample was in cool-down and warm-up stage, and the percent deviation of final mass between Cahn 29 and R-100 balances.....	58
7. $D_o \delta C_o$ from oxide thickness measurements and mass gain curve fitting.....	64
8. D_o from oxide thickness measurements and mass gain curve fitting.....	74
9. Experimental oxide thicknesses and the percent deviation vs. predicted non-isothermal model oxide thicknesses.....	78

LIST OF FIGURES

Figure	Page
1. Partial phase diagram of the oxygen-zirconium system.....	5
2. A schematic representation of oxidation of Zr showing the four regions of oxidation rate.....	7
3. Schematic diagram of surface oxidation on Zr and the processes occurring in the oxide during oxidation.....	15
4. Mechanisms that occur in the surface oxide during the oxidation of Zr.....	17
5. Progression of the oxide-metal interface and the change in O concentration in bulk Zr at points C_n at time θ and points C'_n at time $\theta + \delta\theta$	25
6. Model predicted long term oxygen accumulation during surface oxidation of 0.025 cm thick Zr at 1243 K using a value of $D_o \delta C_o = -1.10 \times 10^{-10}$ mole O/cm sec. Accumulation of oxygen in bulk Zr and oxide layer shown separately.....	29
7. Model predicted surface and bulk oxidation of 0.025 cm thick Zr at 1243 K using a value of $D_o \delta C_o = -1.10 \times 10^{-10}$ mole O/cm sec. The progression of the oxide-metal interface and oxygen concentration are functions of time (in hours)....	30
8. Schematic of the oxidation and saturation system..	33
9. The AES spectrum from 78 eV to 178 eV for: (a) sputter cleaned pure Zr; (b) sputter cleaned Zr:Oss; (c) 10 L O_2 exposed Zr:Oss at room temperature; (d) 300 L O_2 exposed Zr:Oss at room temperature.....	47
10. Mole fraction of O and Zr in Zr:Oss as a function of sputter time.....	50
11. Mole fraction of O and Zr in pure and Zr:Oss as a function of oxygen exposure.....	53

Figure	Page
12. Typical experimental mass gain curve showing the effect of evacuating the system at the start of the run, and returning the system to atmospheric pressure at the end of the run.....	59
13. Experimental and isothermal model mass gains at 1073 K.....	61
14. Experimental and isothermal model mass gains at 1173 K.....	62
15. Experimental and isothermal model mass gains at 1243 K.....	63
16. Experimental and published mass gains; dashed lines this research at (a) 1173 K and (b) 1073 K; solid lines published (c) K. Osthagen et. al. at 1073 K (32), (d) J. Leviton et. al. at 1073 K (6), (e) C.J. Rosa at 1123 K (33).....	66
17. SEM 200X enlargement of polished Zr edge showing surface oxide growth after 6.3 hours at 1173 K in medical grade O ₂	68
18. Experimental and published oxide thicknesses: (a) this research at 1243 K, (b) this research at 1173 K, (c) J.P. Pemsler at 1373 K (34), (d) this research at 1073 K, (e) C.J. Rosa at 1123 K (33)...	70
19. Various diffusion coefficients of O ₂ -in ZrO ₂ : (a) this research from mass gain curve fitting; (b) this research from oxide thickness measurements; (c) and (d) Rosa and Hagel below and above the transition temperature respectively (38); (e) Smith (39); (f) Keneshea and Douglass (15); (g) Madyski and Smeltzer in single crystal near stoichiometric ZrO ₂ (26).....	73
20. Experimental and theoretical mass gains at 1073 K. (a) experimental, (b) isothermal model, (c) non-isothermal model.....	79
21. SEM 200X enlargement of a fractured Zr edge showing surface oxide growth after 10.4 hours at 1173 K in medical grade O ₂	82

Figure	Page
22. Computer Program: Temperature Control in the reactor.....	90
23. Computer Program: Isothermal Model I	91
24. Computer Program: Non-Isothermal Model II	95
25. Computer Program: Model III, Diffusion model to determine the time to reach 99.99% saturation at the midplane.....	99

ABSTRACT

The oxidation of zirconium at high temperatures involves both the formation of a surface oxide and absorption of oxygen into the bulk Zr. The hcp lattice of Zr is reported to absorb up to 29.8 at. % oxygen, which occupies the interstitial sites. The simultaneous surface oxidation and diffusion of oxygen into the bulk Zr were observed at temperatures of 1073, 1173 and 1243 K. Experimental results were compared to predicted results from a model developed here to evaluate values of the oxidation kinetic parameters. Samples of Zr, 0.025 cm thick, were saturated with oxygen by soaking surface-oxidized samples in an argon atmosphere at 1243 K. The initial surface oxidation properties of saturated Zr were compared to pure Zr by AES analysis.

The model of the oxidation process assumes that diffusion of O_2 through the oxide layer is rate limiting. The oxide growth at the oxide Zr interface is described by a mass balance. The principle parameter in the model is the product, $D_o \delta C_o$, the diffusion coefficient of oxygen in ZrO_2 and the oxygen concentration difference across the oxide. The model was calibrated by two completely separate methods. The first compared model predicted curves of mass vs. time to those produced experimentally. The second method compared predicted oxide thicknesses at specific times and temperatures with those observed experimentally. A value for δC_o from the literature was assumed. Then D_o as a function of temperature was determined for both experimental methods. From the mass gain curve fitting method the diffusion coefficient, $D_o = 1.6 \times 10^{-5} \exp(-20700/RT)$ was found. From the oxide thickness comparison the diffusion coefficient, $D_o = 2.0 \times 10^{-2} \exp(-34300/RT)$ was found. It is concluded that the primary oxygen diffusion path is along grain boundaries, and that D_o is a function of extent of oxidation due to changing oxide crystal size during oxidation.

Saturated and pure Zr samples were exposed to successive exposures of O_2 at room temperature, interrupted by sequential AES analysis. Results of the AES study indicate that Zr:Oss surface oxidation is essentially the same as that of pure Zr. The oxygen concentration of sputter-cleaned Zr:Oss was estimated to be 28.8 at. % oxygen by quantitative AES analysis.

INTRODUCTION

Background

Zirconium, Zr, is an abundant metal. However, its use in industry has remained limited. The nuclear industry uses about 90% of the total Zr refined as cladding for fuel rods, and is the largest single industry interested in the properties of Zr. In fact, had it not been for the advent of the nuclear age, Zr would probably be no more than a desk-top curiosity for chemists and researchers. Despite the largely reduced cost, due to the nuclear industry, Zr has found very little use except for a limited amount in the electronics industry.

Zirconium oxide, ZrO_2 , has found extensive use. It is extremely heat and chemically resistant. Hydrofluoric and sulfuric acids are the only chemicals that attack the oxide with any significant effect. Because of these properties, ZrO_2 ceramic tiles can be found in many high temperature applications. The oxide is also an effective catalyst for the coal-gas liquification process, where carbon oxides and hydrogen are passed over ZrO_2 at elevated temperatures resulting in carbon chain formations.

The surface study of catalytic reactions on ZrO_2 present difficulties when certain surface selective spectroscopy methods are used. When the ZrO_2 surface is bombarded with any charged particulate (argon ions, electrons, and etc.), the surface will become charged and deflect the beam. A deflected beam results in interference with the spectroscopy method. To address this difficulty, it has been proposed that surface oxides developed on a Zr metal substrate be used to electrically ground the ZrO_2 study surface. However, heating of the oxide coated metal to catalytic reaction temperatures under ultra-high vacuums results in the oxide layer disappearing. This phenomenon results when the oxygen dissolves into the bulk Zr (1). The dissolution of the oxide surface can be avoided if the oxide layer is grown on an oxygen saturated sample of Zr, denoted as Zr:Oss. Upon further study of this phenomenon, it has been determined to be feasible and valuable to examine the oxide metal interface and learn more about the kinetics of the surface oxidation and the bulk oxygen diffusion process in Zr. The objectives of this study are to produce Zr:Oss samples and to analyze the reaction of oxygen on the surface of bulk Zr.

Related Research

Extensive research has been done on the oxidation of Zr. A majority of the work has been accomplished by researchers in the nuclear industry. They have limited much of their work to conditions achieved in reactors, and usually study Zr alloys. Other research has expanded the knowledge about Zr in conditions other than those in a reactor. Both Douglas (2) and Cox (3) have performed extensive literature surveys. Douglas has compiled a list of observed results regarding kinetics of oxidation and values for the oxidation rate constants. Cox has summarized the theories and mechanisms of the oxidation process. From their work and other publications, a large variation in observed oxidation rates is apparent, as well as a lack of understanding of the mechanisms occurring at the oxide-metal interface.

Many of the general chemical and physical properties of Zr are well known. When Zr is exposed to certain conditions, it is usually predictable how it will respond. On the other hand, it is not clear as to why or by what mechanisms it reacts. Important factors that effect the surface oxidation and the diffusion of oxygen into bulk Zr are temperature, pressure, oxidizing environment, and impurities.

General Characteristics

At room temperature in air, bulk samples of Zr develop a protective surface oxide. On a polished surface, this oxide is about 60 Å thick (4). The cohesive surface oxide blocks the transport of oxygen to the underlying Zr, protecting the metal from further oxidation.

A distinguishing characteristic that separates Zr from many other metals is its ability to form interstitial solid solutions with large amounts of dissolved oxygen. A phase diagram of the oxygen-zirconium system is shown in Figure 1 (5). Recent measurements on this system indicate that a saturated Zr-oxygen solution contains about 29.8 atomic percent oxygen (4).

When a sample of Zr is exposed to oxygen, air, or steam, at elevated temperatures, two processes take place. The oxide layer thickens as the oxide layer's protective abilities are reduced. Simultaneously, oxygen diffuses into the bulk metal. The diffusion process into the metal causes no phase changes when the temperature remains below the α - β transition temperature of 1135 K for pure Zr. Above this temperature, pure Zr exists in the β -phase. The α - β transition is a change in the lattice structure of the Zr from hcp to bcc. As oxygen diffuses into the bulk β -phase, the structure transforms into a stabilized α -phase before the oxygen concentration reaches saturation, as can be seen in the phase diagram.

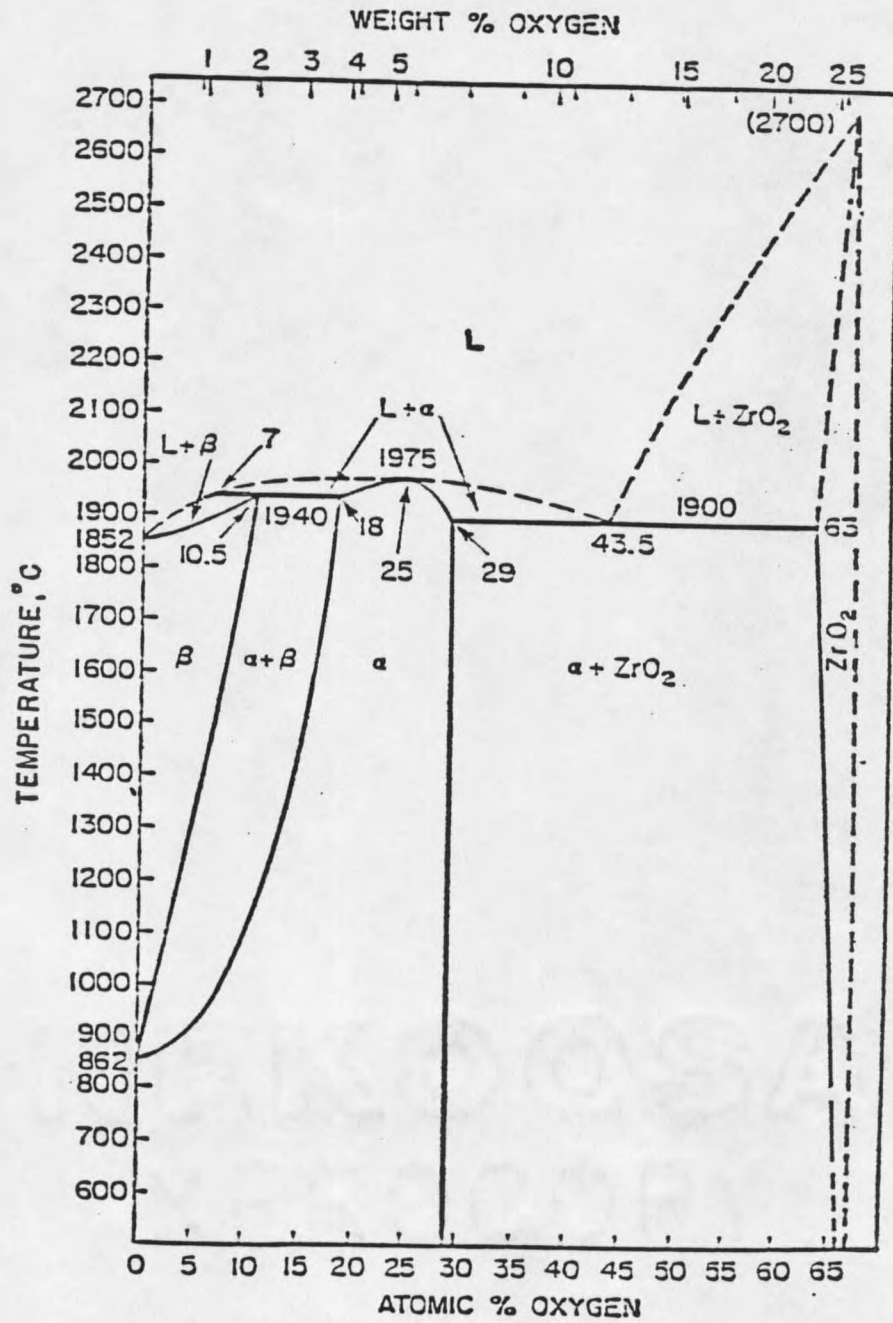


Figure 1. Partial phase diagram of the oxygen-zirconium system (5).

In measurements of the rates of mass gains of Zr at elevated temperatures in oxidizing environments, four regions of oxidation rates are observed (2,3,6). The transitions between the regions are recognized by the change in the rate of mass gain vs. time. A schematic of the transitions and the regions of oxidation are shown in Figure 2 as a plot of mass gain vs. time. The first two regions are observed primarily during low pressure and low temperature oxidation. These regions also occur at high pressures and temperatures, but too rapidly to be easily observed. The first reaction regime is characterized by an unpredictable initial oxidation rate. This region continues up to an oxygen mass gain range of 0 to .01 mg O/cm² of Zr surface. The second transition occurs at about .1 mg/cm², and is associated with a change between different types of second order kinetics. These short term changes in the oxidation rate are not generally noticeable when observing total oxidation extant above about 1 mg/cm². The third transition occurs at various degrees of oxidation, depending on the purity and pre-treatment of the sample.

The first transition is commonly associated with a change in the electrical conductivity of the surface oxide (2,8). The second is associated with the end of a period of amorphous oxide growth and its replacement with non-amorphous black surface oxide (3). The third transition is associated with a physical breakdown of the oxide from black to a white

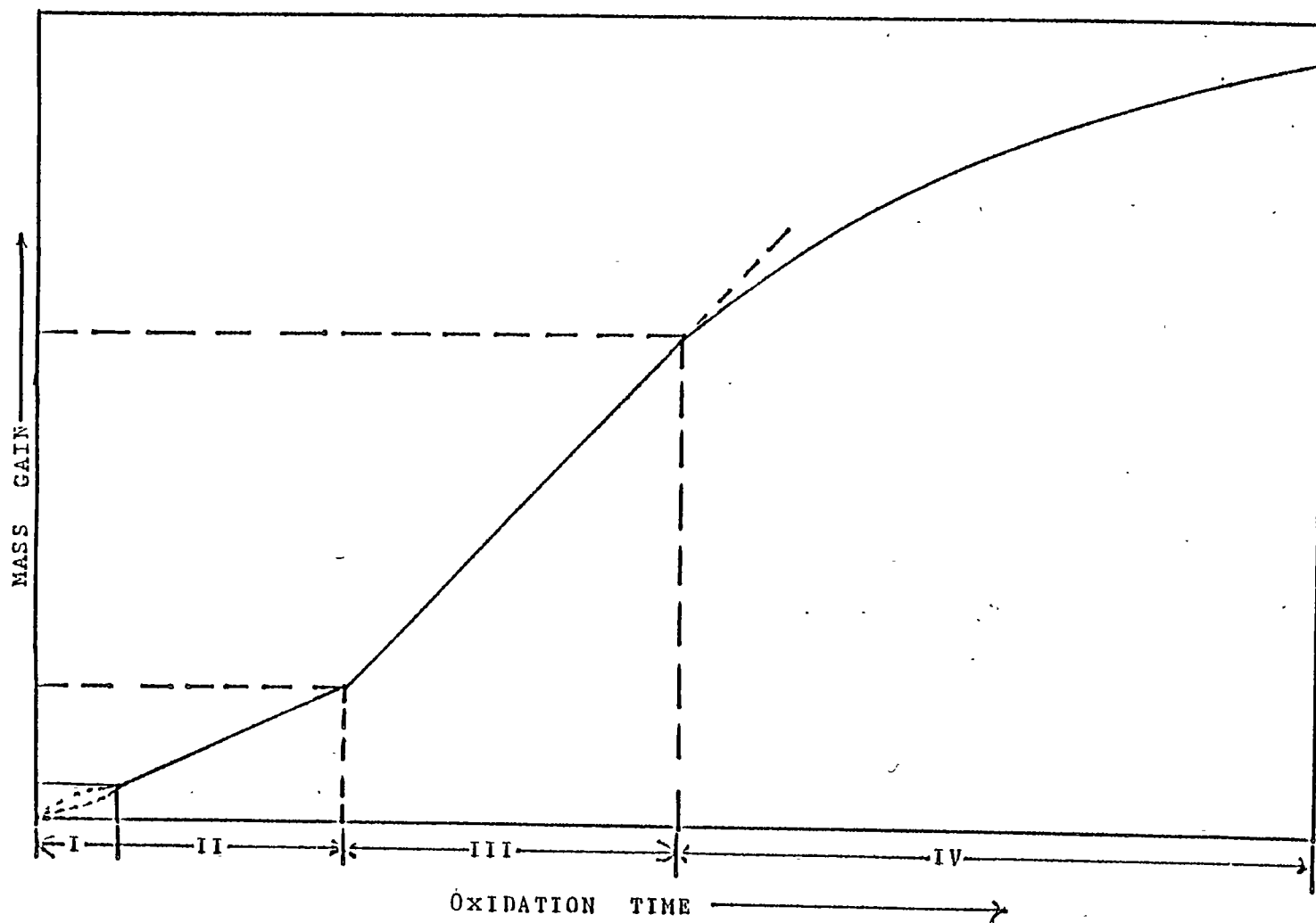


Figure 2. A schematic representation of oxidation of Zr showing the four regions of oxidation rate.

oxide together with flaking or spalling of the surface oxide. The extent of these oxidation regions depends upon the impurities in the Zr sample, as well as the temperature, pressure and oxidizing agent. Below is a description of the effect of each of these parameters on the rate of oxidation of Zr.

Effect of Oxygen Pressure on the Oxidation of Zr. The rate of diffusion of oxygen into Zr has been observed to be independent of O_2 pressure down to about 1 mm Hg (6,7). Below this pressure, the oxidation rate decreases until the pressure is sufficiently low that the oxide dissociates and dissolves into the bulk metal (1). This occurs when the concentration gradient across the oxide becomes sufficiently small that the transport of oxygen across the oxide is less than the rate of oxygen dissolution into the bulk Zr.

The Effect of the Oxidizing Agent. The oxidizing agent has some effect upon the initial rate of oxidation. The effect is only seen in the first two oxidation regions and doesn't significantly influence longer term oxidation. The unpredictability in the initial oxidation rate is believed to be related to the electrical conductivity of the oxidizing agent, the environment with the oxidizing agent and of the oxide layer (8).

Several investigations have shown that the method of surface preparation can strongly effect the initial

oxidation rate (2). This is believed to be due to a change in the conductivity, corresponding to a change in the surface chemical characteristics which are effected by pre-treatments of the surface. It has also been shown that small amounts of impurities may change the initial oxidation rate, probably from a change in the electrical conductivity of the surface oxide.

Diffusion Characteristics

There are many difficulties encountered in the study of the diffusion of oxygen into bulk Zr. Some methods of study have used indirect determination of oxygen content by measuring the microhardness, or the change in the lattice parameters, of the hexagonal close-packed structure (9-13). However, both of these methods are not accurate since neither microhardness nor the change in the hexagonal Zr lattice are directly proportional to the oxygen content in the bulk Zr (4). Direct methods of measurement have employed the etching away of incremented amounts of the surface, followed by the use of nuclear microanalysis to measure the oxygen content of the sequentially exposed surfaces (4). Literature values of the diffusion coefficient of oxygen in Zr are in good agreement with each other. A good average correlation, and the one used in the following analysis is $D_{\alpha} = 5.2 \exp(-50800/RT) \text{ cm}^2/\text{sec}$ (2).

Currently, published diffusion coefficients for oxygen in ZrO_2 are not in as good agreement as those in bulk Zr.

Several problems arise when attempting to evaluate this diffusion coefficient. One complication is associated with the determination of the oxygen concentration gradient through the oxide. Another complication arises from the uncertainty concerning the physical characterization of the oxide.

There have been many attempts to determine the coefficient of diffusion of oxygen in ZrO_2 . One method involves ^{18}O exchange between isotope enriched oxygen and microspheres of ZrO_2 which had been equilibrated at some predetermined oxygen pressure (14,15,16). Another method involves calculating the diffusion coefficient from electrical conductivity data by means of the Nernst-Einstein equation (16). The results from these analysis have good correspondence to a model based on an anti-Frenkle defect structure involving anion vacancies and interstitial anions (3,16). However, it is questionable whether the physical characteristics of the oxides studied are similar to the surface oxide that develops on bulk Zr. It has been demonstrated that the oxide produced on the metal surface has variable physical characteristics depending on temperature, oxidizing agent and environment, impurities in the Zr, and time of exposure to a specific environment.

Surface Science

The advent of surface sensitive spectroscopy methods has brought new direction to the study of the oxide development on Zr. There are many surface spectroscopy methods, including Auger electron spectroscopy (AES) and scanning electron microscopy (SEM) which have been used for Zr oxidation research.

For this work, SEM is used to develop morphological information. The physical characteristics of the surface oxides developed are compared to those found in the literature.

There has been little AES work on the surface oxidation of Zr reported in the literature. One method of AES analysis is associated with depth profiling. Another study technique involves oxidizing the Zr surface by exposing the surface to small amounts of O_2 . From these investigations, three regions of surface oxidation have been observed (17-20). The three regions of initial oxidation all lay within the first two regions shown in Figure 2. They are usually described as the chemisorption range, oxide nucleation range, and oxide thickening range. Samples of Zr have also been lightly oxidized while the sample is resistively heated (19,20,21). However, problems of diffusion of the oxygen into the bulk Zr has made it difficult to observe surface oxidation rates at high temperatures.

In this research, elemental Zr samples are oxygen saturated to form Zr:Oss. The Zr:Oss samples are utilized in an AES study of its surface properties and initial oxidation characteristics. A primary thrust of this investigation is to compare the initial oxide formation on Zr:Oss with that on pure Zr. Future work will involve kinetic studies of surface reactions on an oxide layer formed on the Zr:Oss samples prepared in this work.

RESEARCH OBJECTIVES

The overall goal is to investigate the simultaneous surface oxidation and absorption of oxygen into bulk Zr. Also, develop a method to produce oxygen saturated bulk Zr. The specific objectives were:

1. Prepare a mathematical model of the oxidation process. The model's principle parameters are diffusion coefficients of oxygen in Zr and ZrO_2 and the change in concentration of oxygen through the surface oxide layer.
2. Calibrate the model using experimentally determined values of oxide thickness and mass gain.
3. Prepare Zr:Oss samples.
4. Develop evidence confirming the saturation of the bulk Zr samples by AES depth profiling.
5. Observe the initial oxidation characteristics of Zr:Oss samples by AES and compare the results with the oxidation characteristics of pure Zr.

MODEL DEVELOPMENT

Mechanisms During Surface Oxidation of Zr

There are several physical processes that occur during the oxidation of Zr. These are diagrammed in Figure 3. The entire process can be broken down into several stages. If the rate controlling mechanism is determined and understood, a mathematical representation of the oxidation process may possibly be developed. There are four steps to the oxidation of Zr. First, oxygen must be adsorbed onto the oxide layer where it reacts to form O^{2-} ions. Second, the O^{2-} ions are transported through the oxide layer to the oxide metal interface. Third, the O^{2-} ions react with Zr to form ZrO_2 . Fourth, oxygen diffuses into the bulk metal.

The mechanisms involved with each step must be understood in order to model the oxidation process. It has been shown that the adsorption of oxygen onto the oxide surface is not rate limiting (3). There have also been studies on the diffusion of oxygen into bulk Zr, and the results appear to be consistent since various studies have determined similar diffusion coefficients, as mentioned previously.

The diffusion of oxygen through the surface oxide is assumed the rate limiting step during surface oxidation of

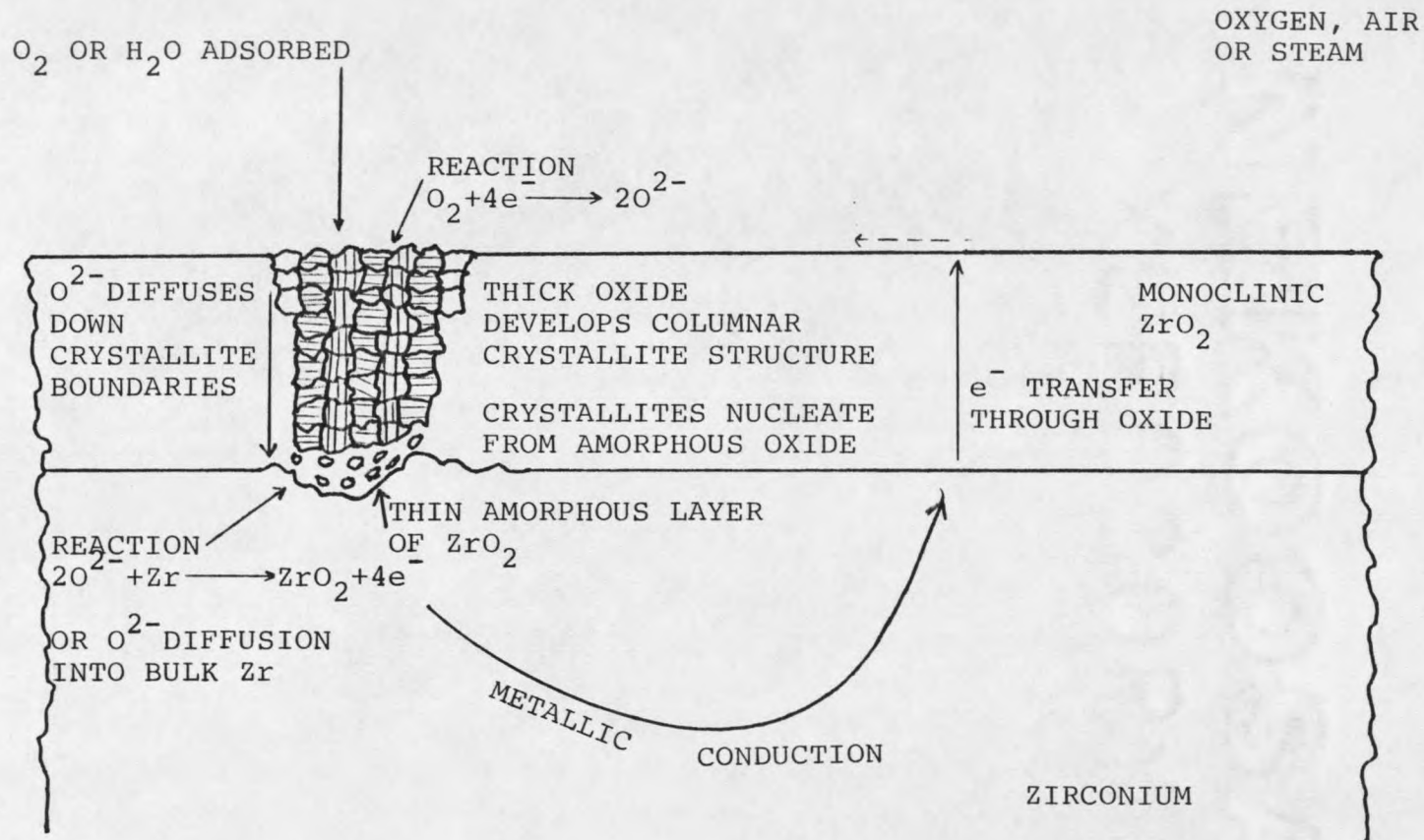


Figure 3. Schematic diagram of surface oxidation on Zr and the processes occurring in the oxide during oxidation.

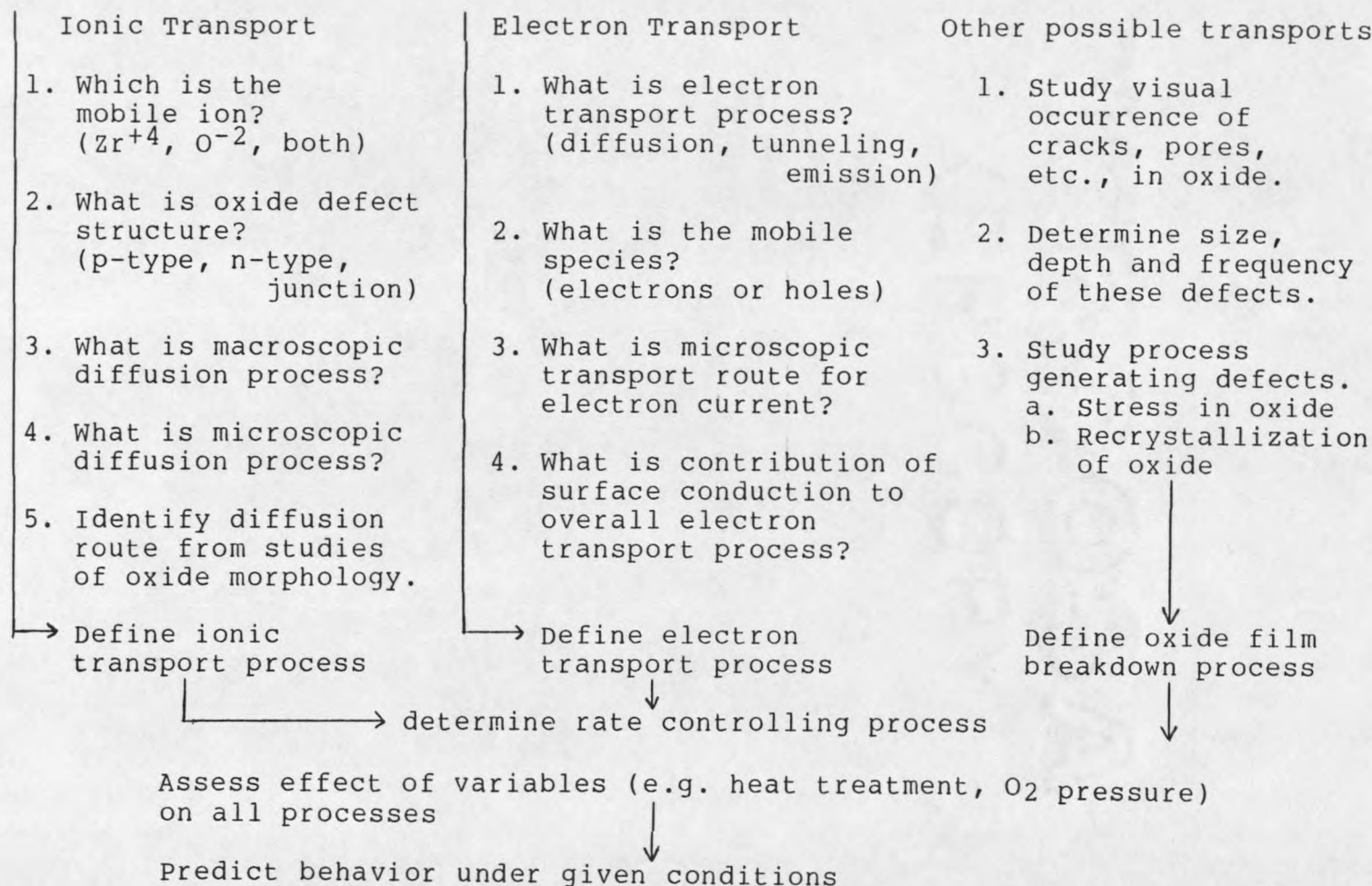
Zr. There are several possible mechanisms for the transport of oxygen through the oxide. Shown in Figure 4 is a list of the important mechanisms that may be involved in the surface oxidation of Zr (3). Figure 4 also suggests procedures for investigating each mechanism. The following is a discussion of the steps outlined in Figure 4, and an interpretation of their importance in developing a satisfactory model.

Ionic Transport in the Oxide

Throughout this analysis, O^{2-} ions have been referred to as the mobile species in the surface oxide. Although, Zr^{+4} could be the mobile ion, studies using injected rare gas atoms have shown that O^{2-} ions are most probably the mobile species (3). Studies of anodic films have shown that movement of Zr^{+4} ions represents less than 1% of the total ion transport (23):

Knowledge of the defect structure assists in the understanding of the method of movement of the mobile O^{2-} species. It has been demonstrated that the defect structure is p-type at pressures near atmospheric, and n-type at pressures below about 10^{-6} atm (24,25). However, these tests were performed on stabilized ZrO_2 samples. It is not clear whether the results apply to thin oxides grown on bulk Zr. There have been many attempts to determine the macroscopic diffusion coefficient of oxygen in ZrO_2 . The most popular and accurate methods involve nuclear reaction of oxygen (22) and $^{16}O/^{18}O$ exchange (26). These methods have been employed

Figure 4. Mechanisms that occur in the surface oxide during the oxidation of Zr.



on a growing oxide on bulk Zr. This eliminates the assumptions about the oxides physical characteristics that must be made when using pure single crystals and polycrystalline spheres of ZrO_2 . There is about a 10^4 order of magnitude increase in the diffusion coefficients found for surface oxides over that of specially prepared bulk ZrO_2 .

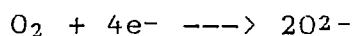
Studies using ion bombardment mass spectrometry have determined that boundary diffusion of O^{2-} in polycrystalline ZrO_2 is a more important transfer method than lattice diffusion (27). The diffusion coefficients determined by the model in the following analysis takes into account both boundary and lattice diffusion. Their combined effect can be described as the effective diffusion coefficient.

An explanation for the second shift in the oxidation rate has been proposed based on the studies of diffusion paths (3). After nucleation and initial oxide growth, the grain boundary size of the oxide crystallites grow by continual recrystallization. At the start of oxidation, up to an oxide thickness of less than 200 \AA , the oxide consists primarily of an amorphous oxide structure (3). Further oxide growth involves the increase in size of the oxide crystals. When the oxide is 1000 to 2000 \AA thick, the crystallites displace the amorphous oxide and occupy 100% of the surface (17-20). As size of the crystallite increases, the area available for boundary diffusion decreases.

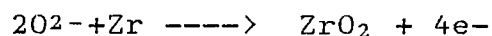
Electron Transport in the Oxide

Figure 3 indicates that the transport of electrons occurs through the surface oxide during the oxidation process. With the use of technology developed in the semiconductor industry, a great deal has been learned about the electron transfer process. The complexity of the electron transfer process is not important to this work, assuming that the electron transfer process is not rate limiting.

The general mechanism involves the adsorption of O_2 on the oxide surface. The most probable surface reaction is:



Oxygen is then transported to the metal-oxide interface where it either reacts or diffuses into the metal. The reaction at this interface is:



The electrons are possibly transported to the surface through several routes (3). Experiments changing the conductivity of the oxidizing environment, and changing the conductivity of the oxide, have indicated that electron transport is not a controlling or a limiting step except, perhaps, during the initial oxidation of the surface. Electron transport no longer influences the rate after a complete oxide has developed over the surface (17-20).

Migration of Oxygen Through the Oxide

Other possible methods of transport of oxygen through the oxide other than lattice or grain boundary diffusion of ions would be the migration of O_2 through cracks and pores. Previous studies predict that for the range of oxygen exposure times and temperatures utilized in this work, few cracks or pores should develop in the oxide layer (2,3). In general, the concentration of cracks increase with temperature, and especially with temperature gradients. Pore formation is common with high content of impurities or with alloying of the Zr. Within the time-temperature parameters of this investigation, these methods of oxygen transport are probably negligible for this work.

Development of a Mathematical Model

From the analysis above, an approach can be defined for the development of a mathematical model of the surface oxidation and bulk oxygen solution process. The transport of O^{2-} ions through the surface oxide is assumed to be rate limiting. The process involves diffusion of oxygen ions from the oxide-gas interface to the metal-oxide interface. The model also assumes the samples to be semi-infinite planes. This assumption is based on the large surface area compared to the thickness of the samples, hence, edge effects are assumed to be negligible.

The computer program modeling the diffusion process is

shown in Appendix 1 as Model I. The model uses the method of lines approach to solve partial differential equations shown in the following sections. The program employs the Differential Systems Simulator version 2 (DSS2). DSS2 is an integration package developed by Dr. W.E. Schiesser in the Chemical Engineering Department at Lehigh University. It has the ability to allow the user a choice of integration methods and control over the degree of relative or absolute error with each iteration. The Gearl Hindmarsh integration method was used which employs a banded approximation of the Jacobian matrix. Output points are found by interpolation.

Adsorption

As stated previously, the surface adsorption process is assumed not to be rate limiting. Hence, the rate of oxygen adsorption onto the oxide surface is assumed greater than the rate of oxygen diffusion through the oxide layer. This was accounted for in the model by giving a fixed oxygen concentration in the oxide at the gas-oxide interface.

Mass Flux Across the Oxide

The oxygen mass flux through the oxide layer is considered to be the rate limiting step and to be diffusion controlled. The differential equation for this process is:

$$N_{\sigma} = -D_{\sigma} \frac{J C_{\sigma}}{J \delta} \quad (1)$$

Where:

N_{σ} - Mass flux of oxygen across the oxide

D_{σ} - Diffusion coefficient of oxygen in ZrO_2

C_{σ} - Concentration of oxygen in the oxide

δ - Depth in oxide

Diffusion of Oxygen into Bulk Zr

The diffusion of oxygen in the bulk Zr metal is determined by assuming unimolecular diffusion in one direction. The partial differential equation for this process is:

$$-\frac{\partial C_{\alpha}}{\partial \theta} = -D_{\alpha} \frac{\partial^2 C_{\alpha}}{\partial X^2} \quad (2)$$

Where:

C_{α} - Concentration of oxygen in Zr

θ - Time

D_{α} - Diffusion coefficient of oxygen in bulk Zr

X - Depth in metal

The mass flux of oxygen into the surface of the bulk Zr is described by the equation:

$$N_{\alpha} = -D_{\alpha} \left. \frac{\partial C_{\alpha}}{\partial X} \right|_{x=\text{interface}} \quad (3)$$

Where:

N_{α} - Mass flux of oxygen into bulk Zr

Interface

The interface equation describes the rate at which the surface oxide layer grows. It is developed with an oxygen balance at the oxide α -Zr interface with the added complication of a density and concentration change. A mass balance between the amount of oxygen transported to the interface through the oxide and the mass of oxygen transported from the interface into the bulk metal is used to describe the mass of oxide growth at the oxide-metal interface. The accumulated oxygen at the interface reacts to form ZrO_2 . The interface is a moving boundary with the rate of oxide growth described by the equation:

$$-\frac{dI}{d\theta} = \frac{(N_{\sigma})_{\text{interface}}}{V \cdot C_{\sigma\alpha}} - \frac{(N_{\alpha})_{\text{interface}}}{C_{\alpha\sigma}} \quad (4)$$

Where:

I - Position of the interface

θ - Time

V - Ratio of density of pure Zr to that of ZrO_2

$C_{\sigma\alpha}$ - Concentration of oxygen in oxide at interface

$C_{\alpha\sigma}$ - Concentration of oxygen in Zr at interface

Solving the equations analytically is tedious, but numerical analysis by a computer simplifies the task and allows manipulation of the boundary conditions.

Since the oxide layer is very thin compared to the bulk Zr, a linear assumption is made concerning the concentration gradient of oxygen through the oxide. Equation (1) then

becomes:

$$N_{\sigma} = -D_{\sigma} \frac{\delta C_{\sigma}}{\delta} \quad (5)$$

and

$$\delta C_{\sigma} = C_{\sigma\alpha} - C_{\sigma g}$$

Where:

δ - Oxide layer thickness

$C_{\sigma g}$ - Oxygen concentration in oxide at gas-oxide interface

The method of lines is used to solve equation (2) using the relationships:

$$\frac{J C_{\alpha}}{J X} = \frac{C_{\alpha(n+1)} - C_{\alpha(n-1)}}{2\delta X} \quad (6)$$

and

$$\frac{J^2 C_{\alpha}}{J X^2} = \frac{C_{\alpha(n+1)} - 2C_{\alpha(n)} + C_{\alpha(n-1)}}{(\delta X)^2} \quad (7)$$

and

$$\frac{J C_{\alpha}}{J \theta} = -D_{\alpha} \frac{C_{\alpha(n+1)} - 2C_{\alpha(n)} + C_{\alpha(n-1)}}{(\delta X)^2} \quad (8)$$

Where $C_{\alpha(n)}$ is the concentration of oxygen in Bulk Zr at some distance δX from the oxide-metal interface at some point n . Demonstrated in Figure 5 is the progression of the models development from point C_0 to point C_N and the change with time $\delta \theta$. DSS2 automatically adjust the size of the change in time $\delta \theta$. The bulk Zr has been divided into equal sized divisions. In the model, the number of divisions is left as a variable. Each point is denoted by C_n where n is a numbered label for each point. The numbering begins with

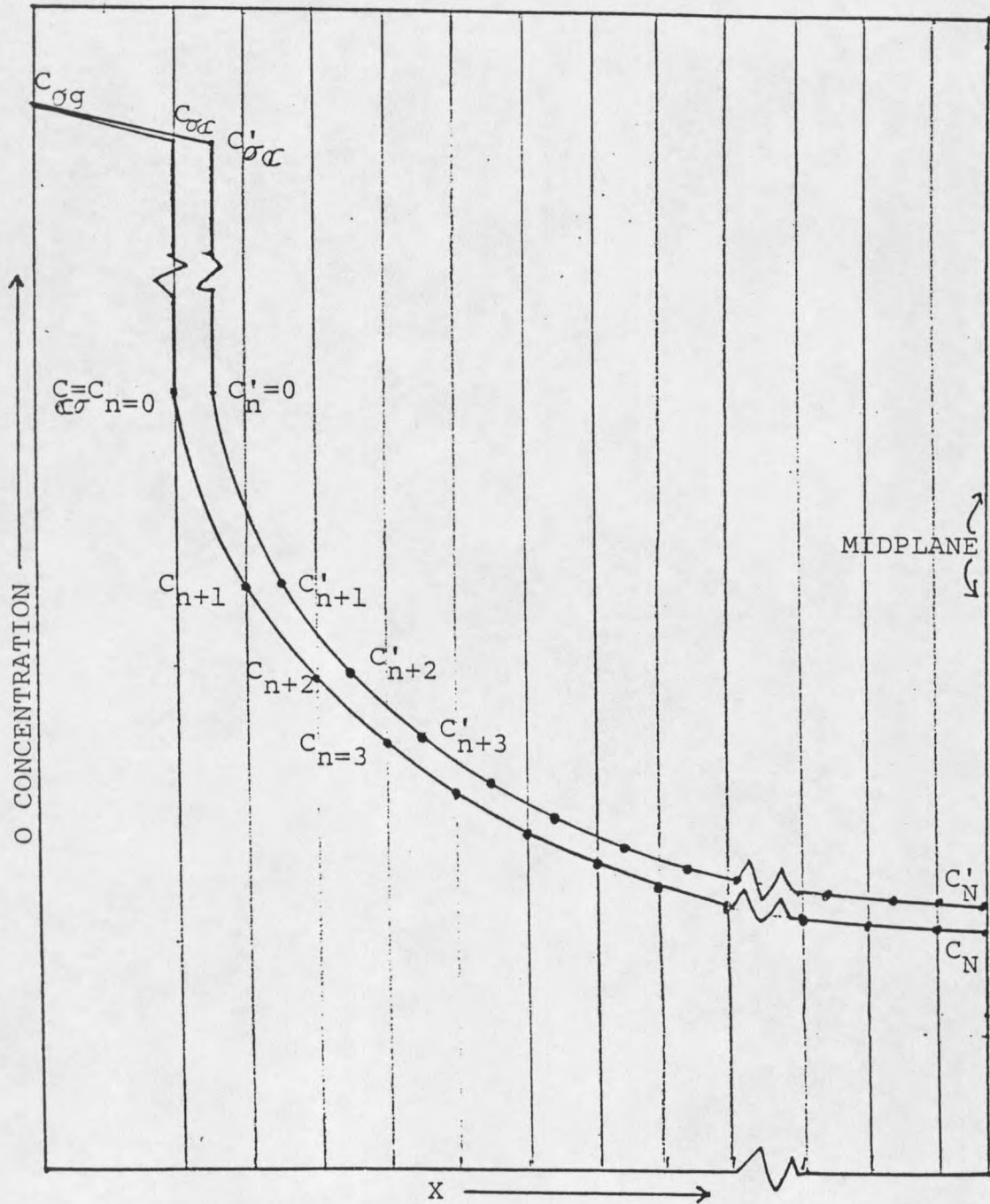


Figure 5. Progression of the oxide-metal interface and the change in O concentration in bulk Zr at points C_n at time θ and points C'_n at time $\theta + 6\theta$.

zero at the oxide-metal interface and ends at the midplane. C_N is the midplane oxygen concentration. As the oxide develops the size δX between each point decreases. Hence, not only is there a change between C_N at time θ and C_N at time $\theta + \delta\theta$, but there is a change in the relative position of C_N . To prevent possible errors that may be caused by the shift in the position of C_N , the relative deviation between each C_N calculated at each time interval was 1.0×10^{-7} .

Boundary Conditions

Initial: $\theta = 0$ $C_\alpha = 0$ for all X

Oxide-Zr interface: at $X=0$, $C_\alpha = C_0 = 0.0302$ mole O/cc

The concentration of oxygen at the oxide-metal interface equal to $C_0 = 0.0302$ mole O/cc is based on three assumptions. First, it is assumed that there must be an oxygen saturated layer in the bulk Zr before oxide can develop and grow. Second, the saturation concentration is 29.8 at.% oxygen. Third, it is assumed that there is no volume change in the bulk Zr metal as oxygen dissolves into the bulk Zr. Therefore, the concentration of oxygen at saturation is the molar density of Zr, times the ratio of moles of O at saturation, to moles of Zr at saturation. If $Zr = 6.49$ g/cc then:

$$6.49 \frac{\text{gm}}{\text{cc}} \times \frac{1 \text{ mole Zr}}{91.22 \text{ gm Zr}} \times \frac{0.289 \text{ mole O}}{0.702 \text{ mole Zr}} = 0.0302 \frac{\text{mole O}}{\text{cc of Zr}}$$

Since the sample is exposed on both sides, there is symmetry at the midplane: $X = N = \text{center}$

$$\left. \frac{J C_{\alpha}}{J X} \right|_{X=N} = 0 = -D_{\alpha} \frac{C_{\alpha(n+1)} - C_{\alpha(n-1)}}{2\delta X} \quad (9)$$

Then

$$C_{\alpha(n+1)} = C_{\alpha(n-1)}$$

and

$$\frac{J C_{\alpha(N)}}{J \theta} = -D_{\alpha} \frac{C_{\alpha(N+1)} - 2C_{\alpha(N)} + C_{\alpha(N-1)}}{(\delta X)^2} \quad (10)$$

$$\frac{J C_{\alpha(N)}}{J \theta} = -D_{\alpha} \frac{2C_{\alpha(N-1)} - 2C_{\alpha(N)}}{(\delta X)^2} \quad (11)$$

The interface equation becomes:

$$\frac{dI}{d\theta} = \frac{-D_{\alpha}(C_{\sigma\alpha} - C_{\sigma g})}{V^* C_{\sigma g} - C_{(0)}} - \frac{-D_{\alpha}(C_{(1)} - C_{(0)})}{\delta X} \quad (12)$$

Where:

$C_{(0)}$ - Concentration of oxygen in Zr at oxide metal interface

$C_{(1)}$ - Concentration of oxygen in Zr at δX from interface.

Variables used in the model are listed in Table 1. The model determines the amount of oxide growth and the proportional amount of bulk Zr reacted to form ZrO_2 . The model then calls the derivative routine to determine the concentration of oxygen through the bulk Zr. With the values calculated from the derivative routine, the model determines

the total mass gain of the sample, mass gain contributed by oxide, and mass gain contributed by oxygen solution in bulk Zr.

Table 1. Variables used in the model.

Variable	Type	Values Used
$D\alpha$	independent	$5.2\exp(-50800/R T)$
$D\sigma\delta C\sigma$	dependent	
T	independent	1073, 1173, and 1243 K
θ	independent	longer then run time
δ -Initial	independent	6.0×10^{-6} cm
V	independent	1.5

Using the values listed in Table 1 and a literature value of $D\sigma\delta C\sigma = -1.10 \times 10^{-10}$ (2) at a temperature of 1243 K, mass gain curves and oxide growth can be calculated by the model. The long term oxidation of a sample illustrating the division of total mass gain of oxygen between the metal and the oxide is shown in Figure 6. The sample would be completely oxidized when the total mass gain curve and the oxide mass gain curve meet. Note that as oxidation continues, the mass of oxygen in the metal decreases as the metal is converted to oxide. This indicates that the model may be effective for long term oxidation, as well as short term, if the correct parameters are used. Figure 7 gives the predicted concentration of oxygen in a sample as a function

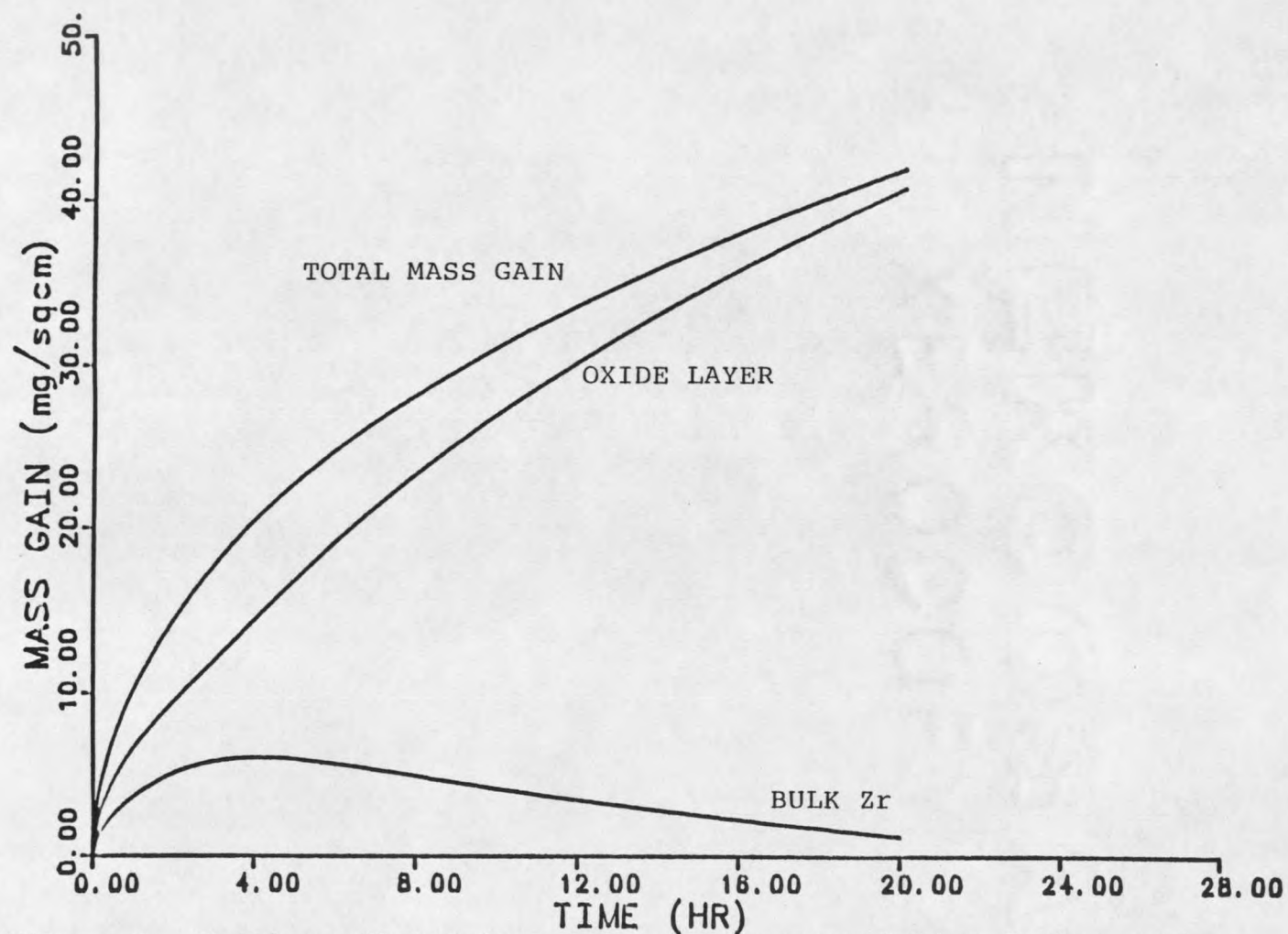


Figure 6. Model predicted long term oxygen accumulation during surface oxidation of 0.025 cm thick Zr at 1243 K using a value of $D_o \Delta C_o = -1.10 \times 10^{-10}$ mole O/cm sec. Accumulation of oxygen in bulk Zr and in oxide layer shown separately.

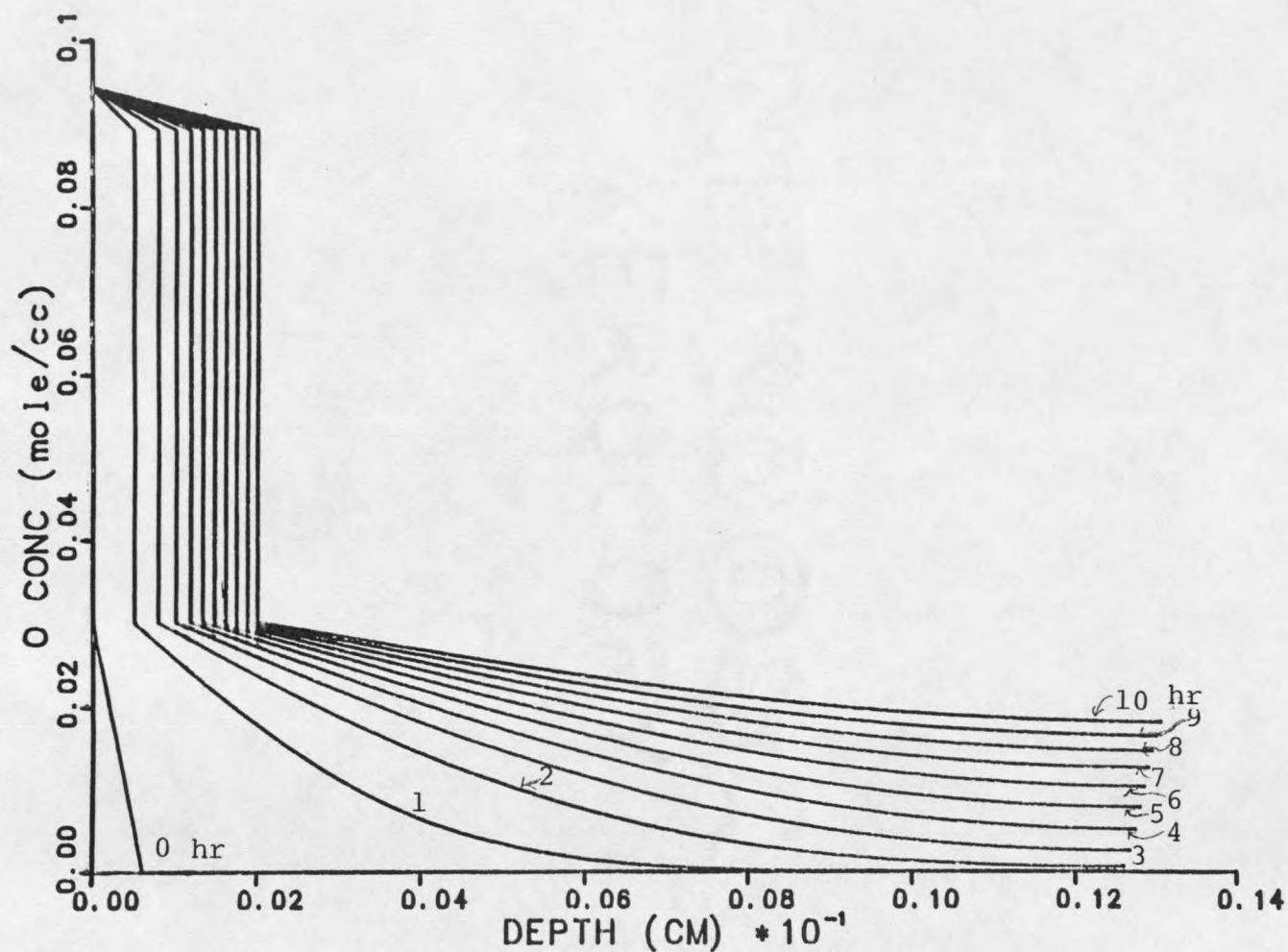


Figure 7. Model predicted surface and bulk oxidation of 0.025 cm thick Zr at 1243 K using a value of $D_O \Delta C_O = 1.10 \times 10^{-10}$ mole O/cm sec. The progression of the oxide-metal interface and oxygen concentration are functions of time (in hours).

of depth for various oxidation times up to 10 hours. Represented on the left hand side of Figure 7 is the gas-oxide interface, which is arbitrarily set at zero depth. The oxide-metal interface is seen to move to the right as bulk Zr is reacted to ZrO_2 . Since there is a density change from Zr to ZrO_2 , the midplane also must move as oxidation occurs, as is shown in Figure 7. As the oxide thickens, the rate of oxide growth decreases, as would be expected.

Utilizing the model to compare oxide growth and mass gains with those determined experimentally, the variable $D_o \delta C_o$ will be determined by matching methods. One method is by manipulating $D_o \delta C_o$ until the oxide thicknesses at specific times and temperatures match experimental values. Another method is a curve fitting technique, in which $D_o \delta C_o$ will be manipulated until predicted total mass gain curves match those measured experimentally.

EXPERIMENTAL EQUIPMENT

Reactor for Oxidation and Saturation of Zr

A schematic of the apparatus utilized to expose Zr to pure O_2 at elevated temperatures is shown in Figure 8. The purpose of the equipment was twofold. The first was to produce Zr:Oss samples. The second was to develop oxide layers on the bulk Zr surface at several temperatures for various lengths of O_2 exposure times. Parameters for the experiment are O_2 pressure, temperature which was controlled by a computer, and duration of the run. Data obtained from the system was mass gain of the sample as a function of time.

The system includes a Cahn/Ventron R-100 null beam electrobalance. The balance detects sample weight gain by application of a counter force to maintain a null position. The counter force is converted to voltage which is recorded by a Varian model 9176 strip-chart recorder. The sample was supported from the beam of the balance by a fine nichrome wire within a quartz tube. A chromel-alumel probe type thermocouple was suspended near the sample. A Linberg single zone tube furnace was used to heat the sample. Isothermal conditions were maintained in the system by use of temperature control by an Apple II computer with a

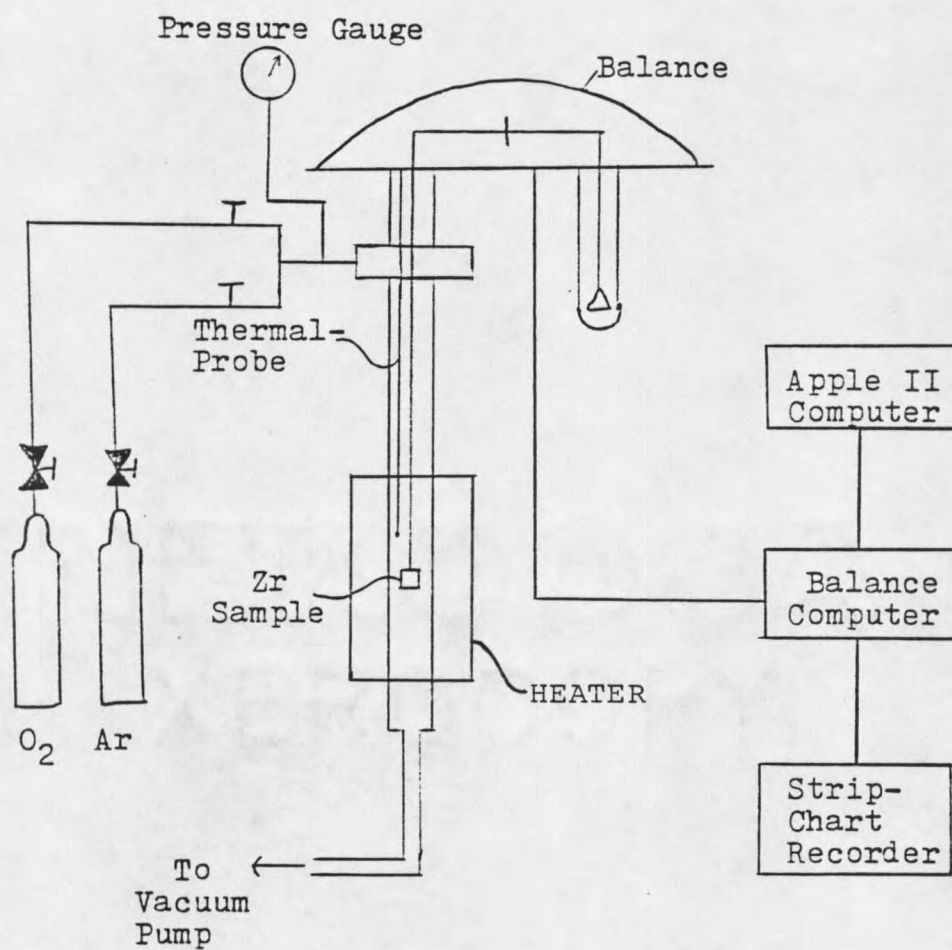


Figure 8. Schematic of the oxidation and saturation system.

Cyborg/Isaac analog-to-digital interface. The computer program used to control temperature is presented in the Appendix. The temperature was controlled to $\pm 1.0^\circ\text{K}$. A Sargent-Welch model 1400 vacuum pump was used in conjunction with needle valves and pressure regulators to control gas inlet and outlet flow. Two pressure gauges were employed to monitor the gas pressures. A Consolidated Vacuum Corporation thermocouple vacuum gauge type GTC-100 was used to measure pressure in the range of 0-1000 microns of mercury. An Ashcroft dial vacuum gauge was used to measure higher pressures.

Surface Spectroscopy Methods

The surface selective spectroscopy methods used were SEM and AES. The following is a description of the equipment and the procedures that were followed in the surface studies.

Scanning Electron Microscopy

SEM was employed to provide morphological information. SEM allows the scanning of very tiny objects. It provides information about the spatial and structural relationships between the oxide and metal. It has several advantages as an imaging tool, including the ability to observe a small point, about 50 Angstroms in diameter, or an area of several square centimeters.

The principal behind SEM when employed as a visual tool

is simple in concept. The surface is rastered with a finely focused beam of electrons. When this beam impinges on the surface atoms, several signals are produced. These include: secondary electrons, backscattered electrons, Auger electrons, characteristic x-rays, and photons of various energies. The secondary electrons are the preferred emission for imaging. They offer higher resolution than backscattered electrons due to enhanced emissions on rough surfaces (28). The detector is sensitive to secondary electrons that escape from the surface with energies of less than 50 keV (29).

The primary electron beam is produced by an electron gun similar to that used in a television tube. The electron beam is rastered across the surface with a computer assisted synchronized pattern which is displayed on a cathode ray tube. The intensity of the moving spot is modulated by monitoring the intensity of the secondary electrons. The primary beam doesn't continuously cover the entire area observed, but moves along the surface in a point by point manner. By this method, an image is produced which can be displayed on the CRT or recorded on photographic negatives. The instrument control is computer assisted, and is operated by an expert technician.

Auger Electron Spectroscopy

Auger Electron Spectroscopy, AES, is a surface qualitative and quantitative analysis technique. It detects the elements that are present within about the first 10

Angstroms of surface. Although AES is not fully refined to its fullest capabilities, it does have the ability to yield chemical bonding information.

The Auger electron is produced in the following manner. The surface of the sample is excited by a primary electron beam from an electron gun. The excitation occurs when an inner core electron is knocked out of its orbit by a primary electron. The excited atom usually relaxes in one of two ways. The atom may have an outer core electron fall into the place of the missing inner core hole, and in this process eject a photon of energy, or it may eject an electron from a core or valence energy level. The ejected electron is a Auger electron. The energy of this electron is characteristic of the element and is effected by the elements environment. The Auger electron is usually denoted by the energy levels that are involved in the process of producing the Auger electron. For example, if an electron was removed from the M level, and one from the N level dropped into its place, a valence, V, electron may be ejected. This process would be denoted as MNV Auger electron.

EXPERIMENTAL PROCEDURES

Oxidation and Saturation Procedures

Two separate oxygen exposure procedures were followed in this research. The first was used to produce Zr:Oss samples. The second was employed to produce uniform surface oxide layers, and obtain total mass gain vs. time data. In both cases the apparatus depicted in Figure 8 was employed. The balance and strip-chart recorder were calibrated using Cahn calibration weights. Periodic checks of the balance indicated that the system remained in calibration throughout the research program. Each sample was pre-weighed and post-weighed on a separate Cahn/Ventron 29 null beam electrobalance accurate to $\pm 1.0 \mu\text{g}$ as a double-check for accuracy of the dynamic mass vs. time measurements.

Sample Preparation

The Zr samples were cut from 0.25 mm thick rolled foil and have a purity of 99.99%. The samples are polycrystalline with a recrystallization texture after rolling which is characterized by a preferential orientation of the $\{10\bar{1}0\}$ planes at 32 degrees with respect to the plane of rolling. The $\langle 1,1,\bar{2},0 \rangle$ direction is parallel to the rolling direction (4). The Zr foil has been examined for bulk oxygen concentration by AES. The oxygen content has been found to

be near zero (30).

Samples of about 1.0 cm X 0.7 cm in size were cut from the foil. Each samples' dimensions were carefully measured to within 0.025 cm. The sequence of sample preparation were as follows.

1. Weigh the sample on the Cahn 29 microbalance.
2. Drill a 0.05 cm hole for the mass balance support wire along one edge.
3. Reweigh on the Cahn 29 microbalance.
4. Etch for 40 seconds in a solution of 60% HNO_3 -35% H_2O -5% HF . The primary etchant in the solution is the HF acid. The nitric acid in this case acts as an oxidizer to slow the etching rate.
5. Stop the etching process by rinsing the sample with distilled water and methanol.
6. Weigh etched sample on the Cahn 29 microbalance.

Experimental Equipment and Procedure

The sample is then suspended from the balance by nichrome wire within the quartz reactor. Each sample underwent the same procedure, the only difference between the saturating process and the oxide growth process is that the saturation process includes an added argon soak period. The procedure is outlined below, with the extra argon soak denoted by asterisks.

1. Tare the R-100 balance to zero.

2. Evacuate the system to less than 1.0 mmHg.
3. Rinse the system with medical grade oxygen.
4. Fill reactor with medical grade oxygen to a static pressure of 206.8 mmHg.
5. Start computer program to begin heating to a pre-programed temperature of 1073, 1173, or 1243 K.
6. Start strip-chart recorder to measure mass gain vs. time.
- *7. At 7.5% mass gain evacuate the system. Rinse with argon, then fill reactor to 620.4 mmHg pressure of argon. Soak in argon at 1243 K. The duration of the argon soak is explained below.
7. Heat the sample at 1073, 1173, or 1243 K for desired length of time or total mass gain.
8. Shut off the heater. When the sample cools to 673 K open the heater to quicken the cooling of the sample.
9. Post-weigh the sample on Cahn 29 microbalance.

Each trial was conducted at an O_2 pressure of 206.8 ± 10 mmHg. This pressure was chosen to be low enough to keep convection currents in the reactor to a minimum and high enough to prevent excessive leakage of air into the system. The O_2 pressure is not critical at this level since the rate of oxidation is independent of pressure above about 1 mmHg. The pressure varied for two reasons. The first is due to the heating of the O_2 in the enclosed system. The second is due to air leakage into the system. Leakage of air into

the system was checked by evacuating the system to 0.1 mmHg and then observing the pressure change with time. The pressure increased at a rate of about 0.033 mmHg/min. At a pressure of 206.8 mmHg there was no measurable change in pressure over 30 minutes time.

Determination of Time to Saturate Samples

For the saturation procedure, a mass gain of 7.5% was chosen to limit the amount of oxide development on the samples' surface. At saturation, 6.9% of the mass of Zr:Oss is oxygen. Hence, a mass gain of 7.5% ensures an excess of oxygen present to diffuse into the bulk Zr during the argon soak. Most of the initial oxygen probably reacts to form a surface oxide which diffuses into the bulk during the argon soak period.

The length of the argon soak was estimated by the computer program shown in the Appendix as Model III to achieve 99.99% midline saturation. This model is the same as Model I shown in the Appendix, and uses the same assumptions, except that it neglects the surface oxide layer. Hence only equation 2 in the model development section needs to be solved. The Zr surface exposed to the gas is assumed saturated as the boundary condition. As a check to the model, Heisler plots which have been developed by analytical solution to equation 2 were also used (31). The model predicted times required to saturate were equal to

those obtained by the Heisler plots. This indicates that the integration section in the models shown in the Appendix are properly calculated.

AES Analysis Procedure

When the samples were removed from the reactor, they were properly labeled and prepared for AES or SEM analysis. The samples that underwent saturation treatment were covered with an oxide layer. This layer was abrasively removed with several grades of silica-carbide paper. The samples were first mounted on a metal holder with thermal set acetone soluble glue. Water was used to flush the samples surface as it was abrasively cleaned. The polishing process went through several grits of 320, 360, 400, 500, 600, 1200, and final polish with 1500 grit. After the final polishing the surface appearance was a shiny metallic. The samples were then chemically etched with 60% HNO_3 /35% H_2O /5% HF solution by rinsing the solution over the samples' surface. The etching process was stopped by rinsing with distilled water. No silica-carbide particles were detected when analyzed for in the AES equipment, indicating that rinsing and etching removed most foreign particles.

The sample thus prepared for AES analysis was then mounted on a special clip designed for use in the AES system located in the CRISS Center at Montana State University. The AES spectra were measured on a Physical Electronics (PHI 595) Scanning Auger Microprobe. Throughout all of the AES

work, the sample was analyzed with a primary electron beam energy of 3.0 KeV with a beam current of 200 na. Two primary regions of Auger electron energy were examined, the region of 78-178 eV for Zr spectra, and the region of 495-515 eV for oxygen spectra.

Two procedures were followed for the AES analysis. One included depth profiling scan. The depth profiling was used to determine when a point was reached in the sample at which there was no longer an oxygen concentration gradient. Depth profiling is achieved within the AES equipment by bombarding the surface with argon ions. The ion bombardment was interrupted by intermediate AES analyses at specific sputter times. Although it is possible to estimate the depth of the sputter, in this case it was not necessary. An important experimental parameter is the control of the ion beam to ensure that a large enough area was sputtered to prevent interference from the edges of the sputter crater during AES analysis. The sputter times were 0.0, 1.0, 2.0, 3.0, 4.0, 5.0, 10.0, and 20.0 minutes with AES analysis between each time interval.

The second AES procedure included the exposure of sputter cleaned pure Zr foil and Zr:Oss samples to successive additions of O₂. Oxygen was exposed at 0.0, 0.3, 1.0, 3.0, 10.0, 30.0, 100.0, and 300 Langmuirs. AES analysis were obtained after each oxygen exposure. A Langmuir is defined as 1×10^{-6} torr.-sec. Table 2 lists the pressure and

length of time that was used to achieve the desired extent of O₂ exposure.

Table 2. Exposure times and pressures utilized in surface oxidation study.

O ₂ Pressure in torr.	Time Exposed seconds	Added O ₂ Exposure	Accumulated O ₂ Exposure
0.0	0.0	0.0	0.0
1X10 ⁻⁸	30.0	0.3	0.3
1X10 ⁻⁸	70.0	0.7	1.0
2X10 ⁻⁸	100.0	2.0	3.0
7X10 ⁻⁸	100.0	7.0	10.0
2X10 ⁻⁷	100.0	20.0	30.0
7X10 ⁻⁷	100.0	70.0	100.0
1X10 ⁻⁶	200.0	200.0	300.0

SEM Analysis Procedure

For this work, the primary goal of SEM was to obtain measurements of the oxide layer thicknesses. This was done for the samples that were not soaked in argon. SEM also yields information about the oxides characteristics, such as the degree of cracking. In this case it was desired to obtain a picture of the magnified sample viewed on edge. The thickness of the oxide could then be accurately determined.

Depending upon length of the heat treatment, the samples ranged from soft to brittle. If a sample was brittle, it was fractured, and the fractured surface was used for SEM analysis. If the sample could not be fractured, it was cut with tin snips. Cutting the sample with tin snips usually damaged the oxide layer. The cut edge was then

polished with silica-carbide paper. The sample was initially polished with 360 grit until no evidence of damage due to cutting was visible. The sample was then polished with 400, 500, 600, 1200, and 1500 grit papers respectively. Water was used to flush the sample and paper. After polishing, the samples were etched in 60% HNO_3 -35% H_2O -5% HF solution for 10 seconds and then rinsed in distilled water. The samples were mounted on holders with a colloidal graphite support. The SEM measurements were performed at the Veterinary Science Department at Montana State University. The samples were magnified 200 times, and polaroid pictures were obtained.

RESULTS AND DISCUSSION

Analysis of Saturated Zirconium

All of the Zr:Oss samples prepared were saturated at 1243 K. Table 3 lists the model predicted time that the samples were expected to reach a midline saturation of 99.99%. Also shown in Table 3 is the actual length of the argon soak. As can be seen, the actual soak times were well beyond the calculated times.

Table 3. Predicted times to reach 99.99% saturation at midplane and actual time of run.

Sample #	Calculated Thickness in cm	Predicted Times to Saturate in Hours	Soak Time Hours
Zr18	0.026	22.9	25.0
Zr19	0.028	25.9	39.0
Zr21	0.027	23.8	40.0
Zr22	0.026	22.9	25.5
ZR23	0.028	25.9	51.0
Zr24	0.027	23.8	30.0
Zr25	0.027	23.8	29.0

Several Zr:Oss samples were produced, one of which was used for AES analysis. The other samples are currently being used or will be used for other research.

The samples were very brittle, and tended to fall apart during the abrasive polishing step. The final size of the

sample used in this work was about 0.25 cm² and approximately one half of the samples original thickness. Visual inspection of the polished surface under a microscope at 10X magnification showed a clean metallic surface.

AES Spectra Analysis by Seah Method

Auger electron spectroscopy was used primarily for qualitative and quantitative measurements of Zr and oxygen concentrations. However, AES spectra is also affected by the bonding relationships between atoms and can yield important information about the chemical characteristics of a surface.

An AES spectra of pure Zr and of Zr:Oss are shown in Figure 9 along with those of Zr:Oss after 10 L and 300 L of O₂ exposure. There are five distinct Zr peaks. They are the Zr89 MNN peak, Zr114 MNN peak, Zr122 MNV peak, Zr138-144 MNV peak, and Zr172 MVV peak. There is only one distinct oxygen peak at 506 eV. The peak intensities were determined, by a computer built into the AES equipment, by measuring the area under the peaks. For this research only the combined Zr138-144 eV peak is used for analysis. There is some controversy in the application of this method when the Zr138-144 eV peak is utilized. As the surface is oxidized, this peak splits, as seen in Figure 9. However, it has been demonstrated that the overall peak intensity is not affected (30). The Zr89 eV peak is not used because of the difficulty in determining where the peak begins from the background spectra. Axelsson

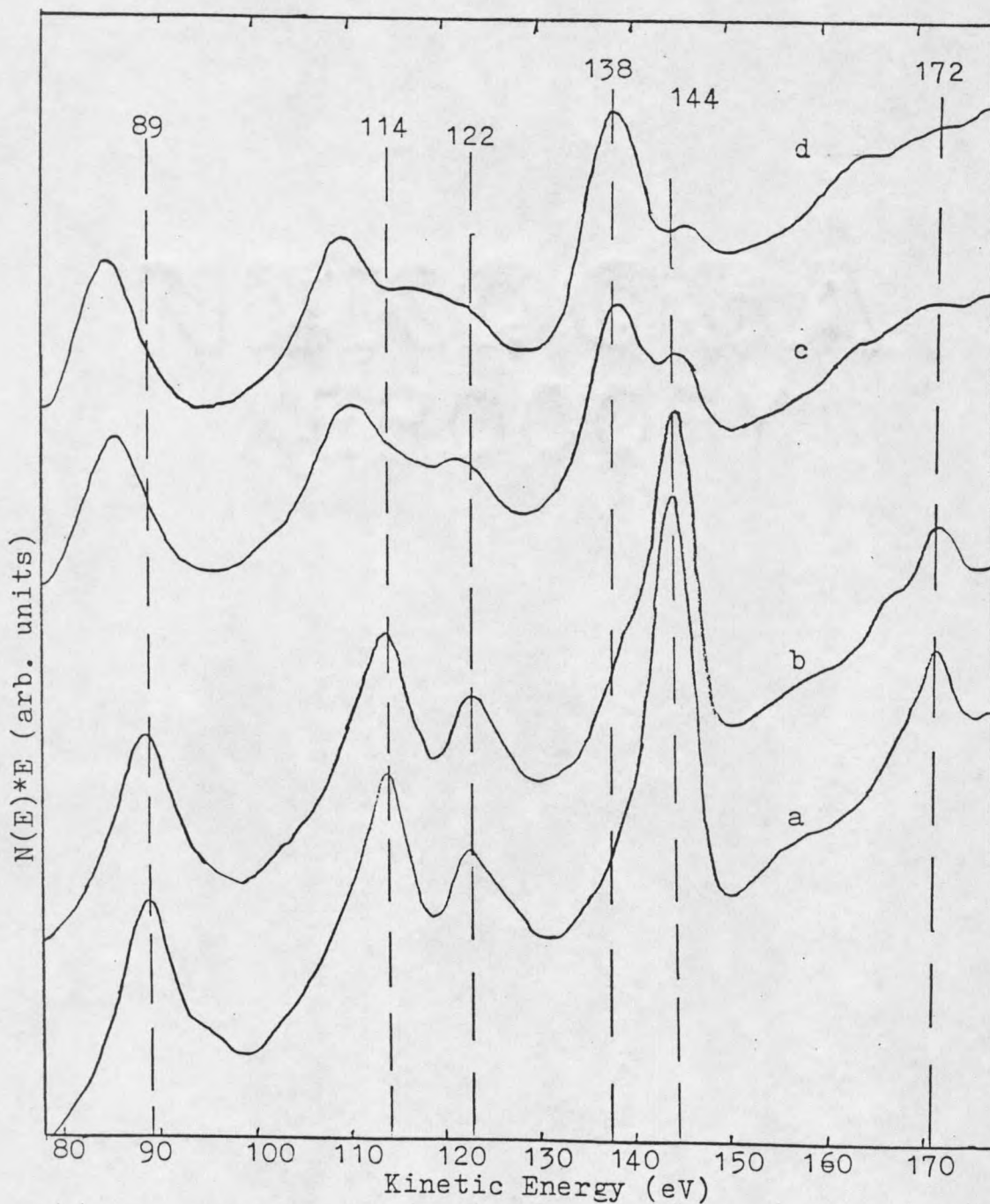


Figure 9 . The AES spectrum from 78 eV to 178 eV for:
 (a) sputter cleaned pure Zr; (b) sputter
 cleaned Zr:Oss; (c) 10 L O_2 exposed Zr:Oss
 at room temperature; (d) 300 L O_2 exposed
 Zr:Oss at room temperature

et. al., estimated that an error of around 15% could result when this peak is used for normalization (17). The Zr114 eV and Zr122 eV peaks overlap making them difficult to use. And the Zr172 eV peak essentially disappears with oxidation.

Peak intensities were converted to mole fractions by the method developed by Seah (40). This is based upon the following relationship:

$$\frac{I_o}{I_{Zr}} K = \frac{X_o}{X_{Zr}}$$

Where:

I_o - O₅₀₆ peak intensity

I_{Zr} - Zr peak intensity

K - Proportionality constant

X_o - Mole fraction of oxygen

X_{Zr} - Mole fraction of Zr

Seah has demonstrated that in many instances the ratio of peak intensities is proportional to the ratio of mole fractions. Deibert has demonstrated that this holds for Zr (30).

The constant K is evaluated by the following method. For stoichiometric ZrO₂, the mole ratio is:

$$\frac{X_o}{X_{Zr}} = \frac{2}{1}$$

The Zr138-144 eV and O506 eV peak intensities were measured after 100 L of oxygen exposure to the Zr:Oss sample. It has been demonstrated that the surface of Zr is stoichiometric ZrO₂ after 60 L of oxygen exposure (17-20). However, the

mean escape depth for the 506 eV oxygen peak is 3 times that of the Zr peaks (21). Hence, it is important to be certain that the oxide layer is thick enough to produce the desired ZrO_2 spectra. It is assumed here that the spectra after 100 L of exposure is that of ZrO_2 . The peak intensities measured after 100 L O_2 exposure were:

$I_o = 53520$ counts

$I_{\text{Zr}138-144} = 12690$ counts

Then $K = 0.47$ Dimensionless

This value of K is used through the remainder of this report to determine Zr and O concentrations from AES peak area intensities.

Depth Profile

A depth profile of the Zr:Oss sample was produced by sputtering the surface with argon ions. In this case it was not important to determine the depth of sputter as a function of time, it was only necessary to determine that the Zr:Oss sample was saturated. This is accomplished by demonstrating that the AES spectra no longer changed with continued sputtering. Also it may be demonstrated that the concentration of oxygen and Zr on the sputtered surface is close to the saturation concentration of 29.8 at% oxygen. The concentration of oxygen and of Zr as a function sputter time is shown in Figure 10. The sample was sputtered for a total time of 20 minutes. After 5 minutes of sputtering the

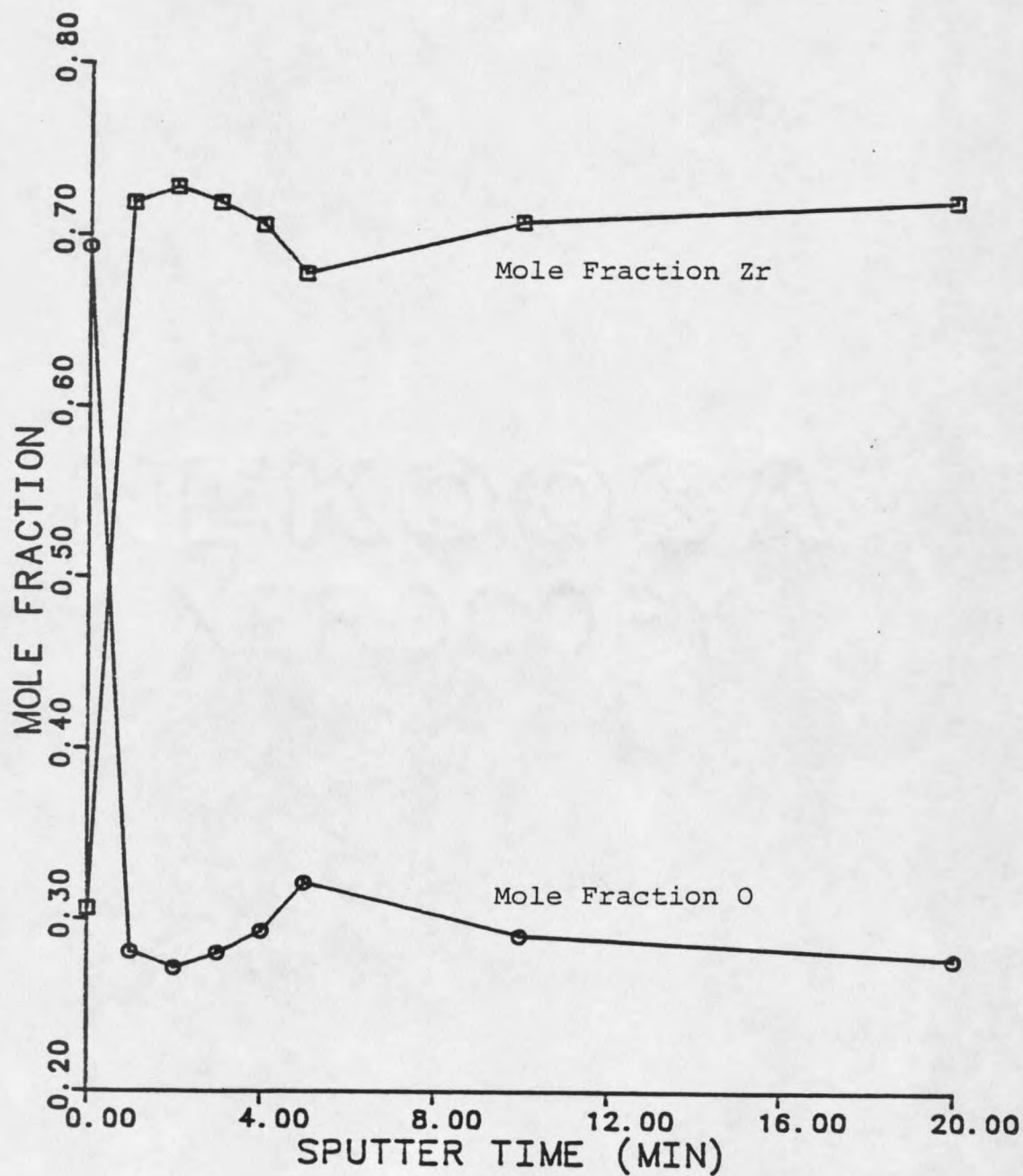


Figure 10 . Mole fraction of O and Zr in Zr:Oss as a function of sputter time.

oxygen concentration appears to slowly decrease. This indicates that the sample may not be saturated. However, further experimental work, accomplished at Montana State University, using the Zr:Oss samples developed here has demonstrated that the samples are probably saturated.

To prove saturation of the Zr:Oss samples produced in this work, Kahraman et al, grew thin oxide layers on the Zr:Oss samples and heated them to 1200 K for 5 minutes and 900 K for one hour (21). In both cases the oxide thickness did not change, indicating that the samples were saturated. Had the samples not been saturated, the oxide layer would have been absorbed into the bulk Zr.

Using Seah's method to analyze the peak intensities from depth profiling, it is possible to obtain the concentration of O and Zr in the sputter cleaned Zr:Oss sample. The mole fractions of O and Zr are 28.8 atomic percent and 71.2 atomic percent respectively. This is close to the published values of 29.8 atomic percent and 70.2 atomic percent for O and Zr, respectively.

Initial Oxidation at Room Temperature

The initial oxidation characteristics of Zr:Oss were compared to that of pure Zr. Whatever steps were performed on the Zr:Oss sample were also performed on a pure Zr sample. After the sample was milled clean by rastering the surface with argon ions, successive additions of oxygen were

exposed to the surface at room temperature. This was accomplished by opening an oxygen valve leading to the AES chamber. The pressure was increased to a set point for a set length of time to allow exposures of 0.3, 1.0, 3.0, 10.0, 30.0, 100.0, and 300.0 Langmuirs. There are several combinations of times and pressures to attain a certain extent of O_2 exposure. It has been demonstrated that if different times and pressures are used to reach the same extent of exposure, different AES spectra are produced (21). The changes are minor, and probably do not interfere with this analysis. Table 2 lists the times and pressures used to achieve the desired exposures. After each exposure, the sample was analyzed in the energy ranges of 78-178 eV for the Zr spectra, and 495-515 eV for the O spectra. Table 4 is a list of the peak area intensities calculated by the computer built-in to the PHI 595 system. Following Seah's procedure described above, and using the Zr139-146 eV and the O506 eV peak intensities a comparison between the oxidation characteristics of pure and saturated Zr was made.

The mole fraction of oxygen and of Zr as a function of the extent of O_2 exposed are shown in Figure 11. Both the saturated Zr and pure Zr curves are shown with dotted and continuous lines, respectively. The Zr:Oss curve starts at 27.8% O and approaches the saturation value of 67% O which was used as the calibration point. The pure sample starts at about 0.0% O and approaches 67% O at a slightly larger

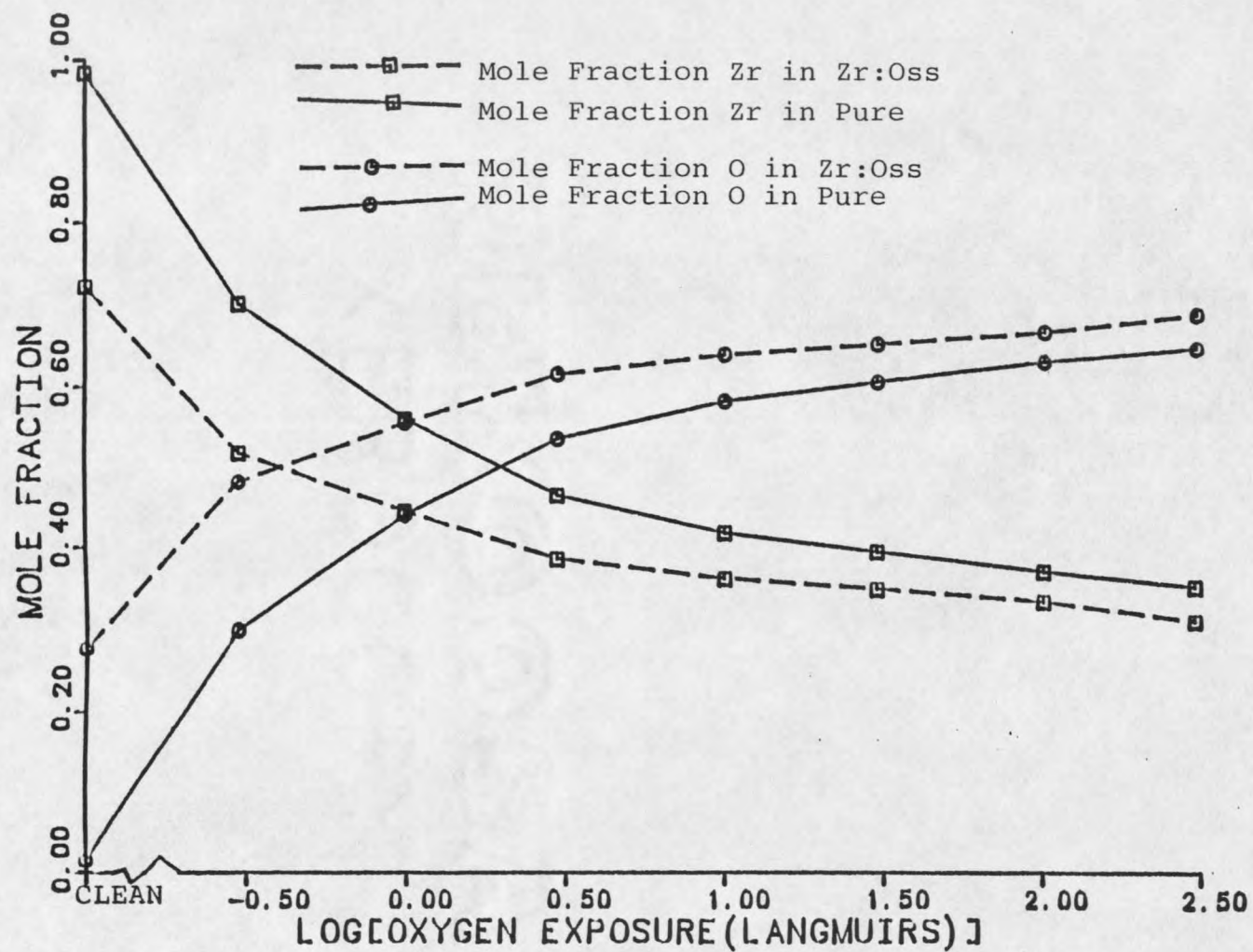


Figure 11. Mole fraction of O and Zr in pure and Zr:Oss as a function of oxygen exposure.

extent of O_2 exposure. The end result is that the saturated sample and the pure Zr appears to oxidize in similar fashions at room temperature.

Table 4. AES primary peak intensities for pure and Zr:Oss.

Trial	Langmuirs of O ₂	AES Peak Intensities eV			
		Zr89	Zr139-146	Zr172	0516
Zr:Oss					
TZSM08	0.0	11155	18690	3761	15150
TZSM09	0.3	9785	15679	2381	30840
TZSM10	1.0	8780	14783	1635	38996
TZSM11	3.0	8376	13624	902	45851
TZSM12	10.0	8295	13106	672	48951
TZSM13	30.0	8075	13120	431	51704
TZSM14	100.0	7912	12690	192	53520
TZSM15	300.0	7628	13002	0	60774
Pure Zr					
TZPM03	0.0	11936	21346	4634	717
TZPM04	0.3	11396	18891	3391	17020
TZPM05	1.0	10249	17019	2507	49847
TZPM06	3.0	9583	15586	1555	37895
TZPM07	10.0	8996	14759	1023	43431
TZPM08	30.0	8877	14584	748	47260
TZPM09	100.0	8453	13963	450	50248
TZPM10	300.0	7786	13155	255	51093

Diffusion Coefficient Determination

The model is used to estimate values of $D_o\delta C_o$ by matching predicted to experimental oxide thicknesses and mass gain curves. When values of $D_o\delta C_o$ are obtained, they are evaluated for accuracy. The discussion of the model results is divided into four sections. The first section introduces some of the models deviations from reality, and

the steps that have been taken to account for the deviations. The second section discusses the results obtained from the curve fitting technique. The third section discusses the results observed from the oxide thickness matching technique. The fourth section compares the results to literature and discusses the meaning and importance of the results.

The model matching techniques of mass gain curve fitting and oxide thickness matching are independent of each other. The only factor that links them is that the experimental data for each method was obtained from the same Zr samples. In the following discussion, the results from each technique is treated separately, and will later be compared to each other.

Model Application

Model I shown in Appendix 1 is an isothermal model of the oxidation-diffusion system. Model I was used to determine the values of $D_o \delta C_o$ by the two methods of curve fitting and oxide thickness matching. However, the experimental system in actuality is not isothermal. The system requires approximately 35 minutes to go from room temperature to 1243 K. About the same amount of time is required for cooling. In using the isothermal model, error is involved by determining the point at which time must start and stop with the experimental data. Time was started when the reactor temperature reached 873 K, and the run time

ended when the reactor temperature cooled to 873 K. A temperature of 873 K was chosen by assuming that very little oxidation or diffusion occurred below this temperature, and that the rate of oxidation and diffusion remain constant during the temperature transition from steady state to 873 K. The experimental system required approximately 6 minutes to warm up to 873 K, and about 10 minutes to go from 873 K to room temperature.

To determine the effect of ignoring the warm up temperature transition, the results from the isothermal model were used in a non-isothermal model. The non-isothermal model is shown in Appendix 1 as Model II. Time-temperature data was obtained from the experimental system. To develop the non-isothermal model, the values of $D_o \delta C_o$ found in the isothermal model were used to calculate D_o as a function of temperature. Then D_o values as a function of temperature were used in the non-isothermal model. The change in results between the non-isothermal model mass gain predictions, and oxide thickness predictions with experimental values, will establish the degree of error due to warm up effect.

Table 5 lists the trial numbers and the exposure conditions for each sample. The total experimental time started when the temperature in the reactor reached 873 K. The system was very consistent at warming up at the same rate for each trial. The percent of the total time that is

warm up and cool down time is least for the longest runs, but is as high as 46% for the shortest run. This is especially significant in the runs at 1243 K. The percent of the run time that is cool down and warm up time is listed in Table 6, together with total mass gain measurements by the R-100 balance and the Cahn 29 balance, and the deviations between the two methods.

As mentioned in the introduction, the initial rate of oxidation varies with reactor conditions. For this work, each sample has a high purity and each went through the same pre-treatments. It is therefore assumed that the rate of oxidation was equal for each sample under similar conditions. The length of the runs in this work were long enough to avoid interference from the first two oxide development transitions, but short enough that the oxide growth didn't approach the third, oxide break-down, stage.

Table 5. Oxidation conditions of each zr sample.

Run #	Experimental Run Time in Hours	Total Area cm ²	O ₂ Pressure mmHg	Temperature K
Zr38	6.9	0.989	207.6	1073
Zr39	10.0	0.991	207.6	1073
Zr37	2.1	0.985	207.8	1173
Zr36	4.1	1.068	207.3	1173
Zr34	6.3	1.047	206.8	1173
Zr35	8.2	1.087	206.8	1173
Zr33	10.4	1.422	206.8	1173
Zr40	1.8	1.096	206.8	1243
Zr41	2.7	1.108	206.8	1243

Table 6. Percent of total time sample was in cool-down and warm-up stage, and the percent deviation of final mass between Cahn 29 and R-100 balances.

Run #	Total Experimental Time (Hour)	% Time at Non-steady State	Final Mass Gain		% DEV.
			Cahn 29 (mg)	R-100 (mg)	
Zr38	6.9	8.4	*11.659	13.69	17.4
Zr39	10.0	12.1	6.270	6.33	1.0
Zr37	2.1	40.0	5.330	5.17	3.0
Zr36	4.1	20.4	8.190	8.62	5.3
Zr34	6.2	13.4	9.914	11.01	11.0
Zr35	8.2	10.3	13.627	14.65	7.5
Zr33	10.2	8.1	*17.481	21.79	19.7
Zr40	1.8	46.0	10.146	10.97	8.1
Zr41	2.7	34.0	*7.702	16.63	115.9

* Cahn 29 mass measurements are not accurate due to loss of mass from the samples during removal from reactor.

Isothermal Model Correlations from Curve Fitting Methods

The experimental mass gain curves used in the curve fitting process were obtained from the strip-chart recorder system described in the experimental section. A typical experimental mass gain curve is shown in Figure 12. During the initial heating, a sharp jump in mass is detected equivalent to about 1 mg. This occurred right after the system was evacuated and then filled with oxygen. At the end of the curve is an equivalent sharp drop in mass. This occurred when the system returned to ambient conditions. It was also noticed that when the quartz tubing was raised around the sample, the sample had a tendency to cling to the walls of the quartz reactor, probably due to static charges.

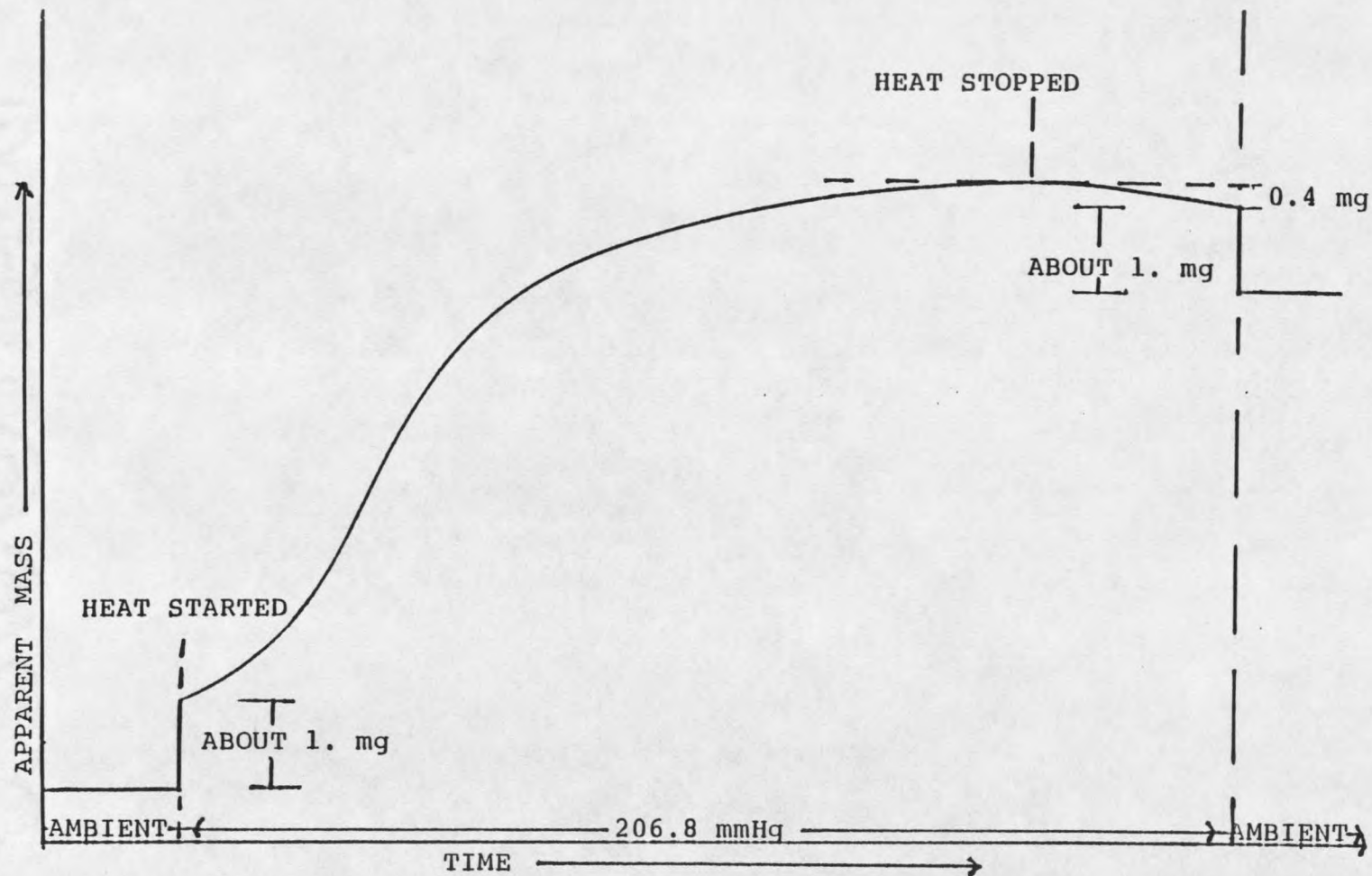


Figure 12. Typical experimental mass gain curve showing the effect of evacuating the system at the start of the run, and returning the system to atmospheric pressure at the end of the run.

Although the sample itself was grounded, an induced charge may have been placed on it from the charged and insulated quartz reactor walls. The two jumps in mass are probably due to the change in the static forces with a change in pressure. The point at which the heater was turned off is marked in Figure 12. As the reactor temperature cools, there is a decrease in apparent mass. It decreases a total of about 0.4 mg from the start of cooling to the time that room temperature is reached. This decrease in mass is probably due to a change in convection currents as the system cools.

Evaluation of $D_o\delta C_o$ from Curve Fitting. In developing experimental mass gain curves the mass change due to the static forces was subtracted from the plotted curves to produce an adjusted mass gain curve. The model was fitted with the adjusted curves. The experimental mass vs O_2 exposure time curves at temperatures of 1073, 1173 and 1243 K are plotted in Figures 13-15, together with the mass gain predicted by the isothermal model. The dashed lines are the experimental mass gain curves. Two experimental curves were produced at 1073 K and 1243 K, and five experimental curves were produced at 1173 K. The solid lines are the curves produced from the model. They include total mass gain, mass gain due to oxide growth, and mass gain of oxygen in the bulk metal. The parameter $D_o\delta C_o$ is adjusted in the model until the model total mass gain curve has the best visual fit with experimental mass gain curves. The values of $D_o\delta C_o$

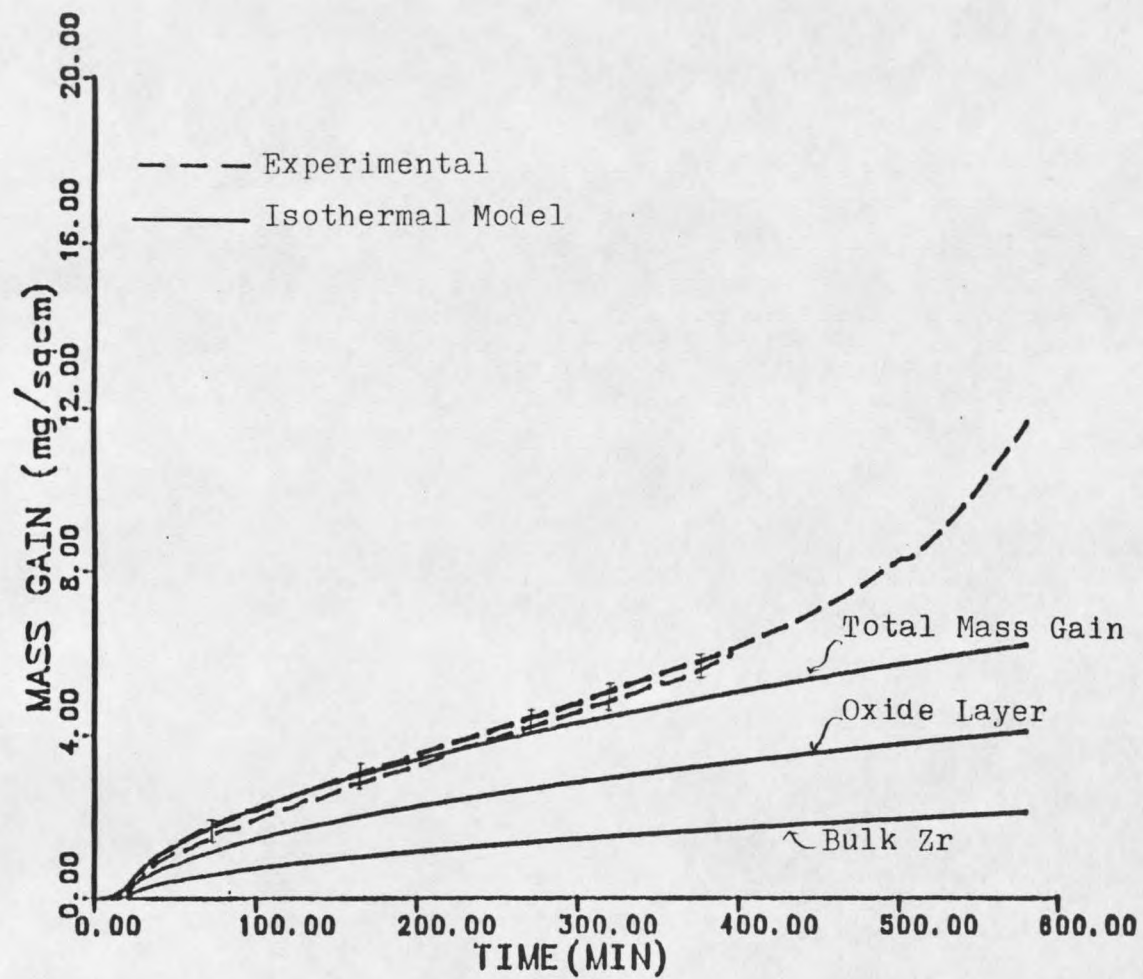


Figure 13. Experimental and isothermal model mass gains at 1073 K.

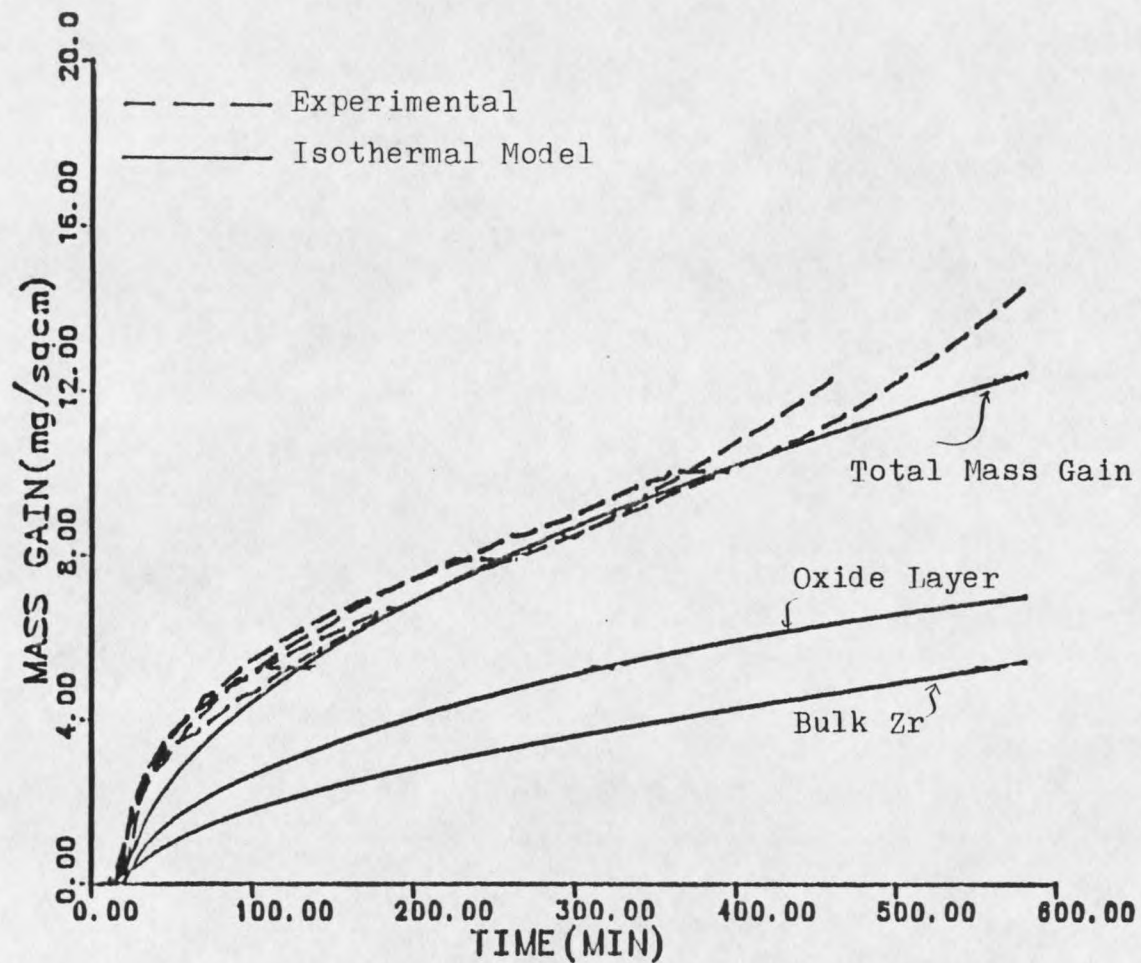


Figure 14. Experimental and isothermal model mass gains at 1173 K.

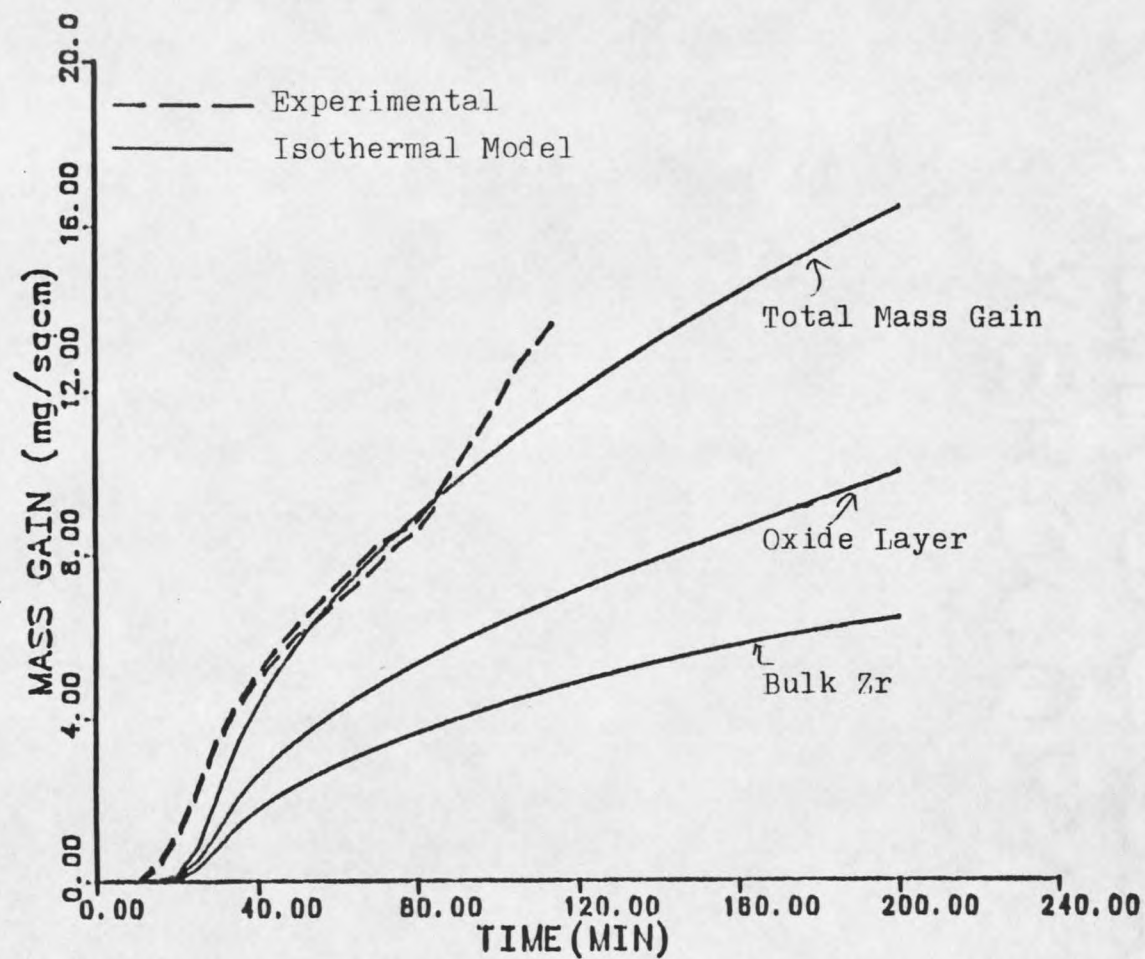


Figure 15. Experimental and isothermal model mass gains at 1243 K.

found at the three temperatures by this method are listed in Table 7. Also shown in Table 7 is $D_{\sigma}\delta C_{\sigma}$ estimated from the oxide thickness measurements, which will be discussed in the following section.

Table 7. $D_{\sigma}\delta C_{\sigma}$ from oxide thickness measurements and mass gain curve fitting.

Run #	Time Hours	Temp. K	$D_{\sigma}\delta C_{\sigma}$ From Oxide Thickness mole O/cm sec	$D_{\sigma}\delta C_{\sigma}$ From Curve Fit mole O/cm sec
Zr38	6.9	1073	-1.02×10^{-11}	-4.53×10^{-12}
Zr39	10.0	1073		
Zr37	2.1	1173	-5.12×10^{-11}	-1.14×10^{-11}
Zr36	4.1	1173	-3.93×10^{-11}	
Zr34	6.3	1173	-3.49×10^{-11}	
Zr35	8.2	1173	-3.37×10^{-11}	
Zr33	10.4	1173	-2.93×10^{-11}	
Zr40	1.8	1243	-1.14×10^{-10}	-1.10×10^{-10}
Zr41	2.7	1243	-1.10×10^{-10}	

Experimental Errors Involved with Curve Fitting. The experimental error involved with the mass vs. time data was estimated by comparing the final mass of the samples recorded on the R-100 and the Cahn-29 balances. Table 6 lists the deviation in final masses between the two balances for each trial. The large deviation in trials Zr33, Zr38, and Zr41 is due to loss of oxide from the edges of the samples as they were removed from the quartz reactor. The experimental mass gains are estimated to be accurate to ± 1 mg. Since an error of ± 1 mg is greater than the deviation

of 0.4 mg caused by convection currents, convection forces do not significantly interfere with the analysis.

Other possible errors associated with this analysis include accuracy of matching two differently shaped curves. An error of ± 1 mg translates to an error of about ± 0.7 mg/cm² of Zr surface. This range of error has been marked in Figure 13. Most of the experimental mass gain curves lay within the estimated experimental deviation. Since the model curve doesn't have the same shape as the experimental curves, it is only possible to fit part of the predicted curve to the experimental curves. This can be observed in Figure 13 where the model curve does not lay within the marked deviations at all points. The end result is that the $D_G \delta C_G$ values found by the curve fitting method are not very precise, and the errors can not be easily quantified.

Several previously published mass gain curves are compared to those obtained here in Figure 16. Curve (c) is produced from experimental results of Osthagen et. al. at 1073 K (32), curve (d) from experimental results of Leviton et. al. at 1073 K (6) and curve (e) from experimental results of Rosa at 1123 K (33). The dashed lines are the experimental mass gains found from this work at 1073 and 1173 K. The initial section of the mass gain curves developed in this work follow closely with those previously published. However, at as early as 200 minutes the rate of mass gain starts to increase above those previously

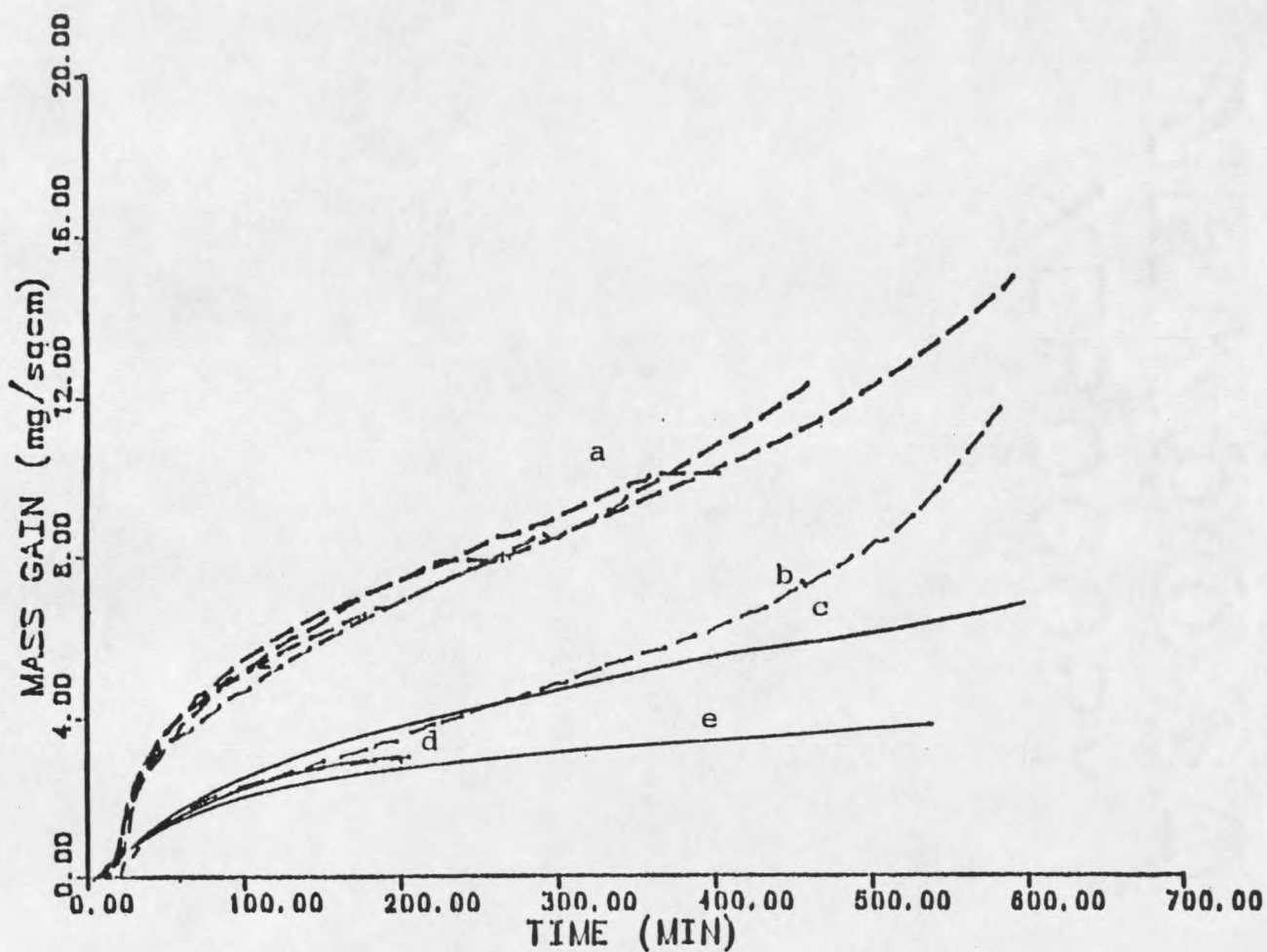
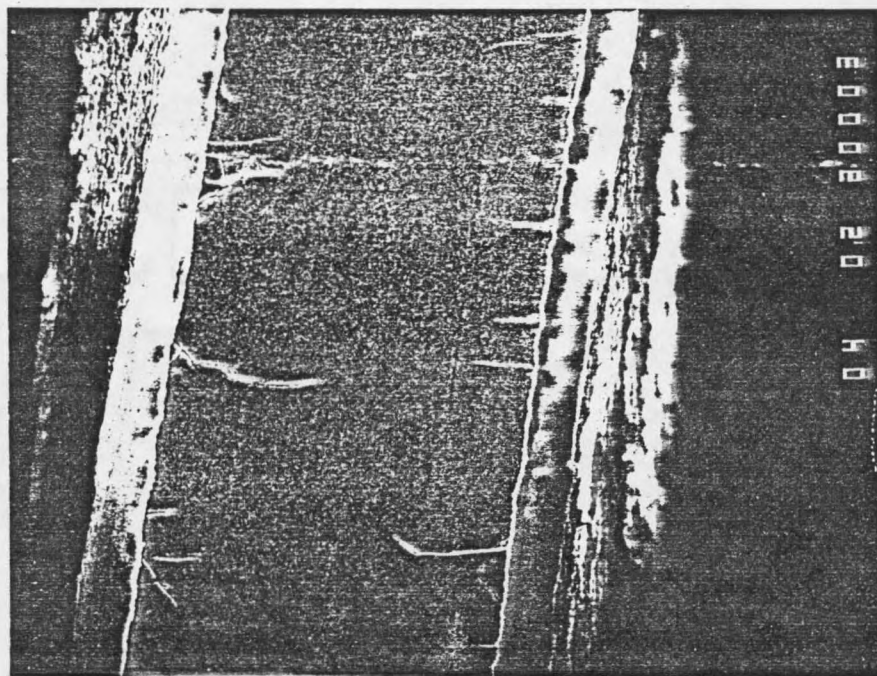


Figure 16. Experimental and published mass gains; dashed lines this research at (a) 1173 K, and (b) 1073 K; solid lines published (c) Osthaen et. al. at 1073 K (32), (d) Leviton et. al. at 1073 K (6), (e) Rosa at 1123 K (33).

observed. This type of behavior is usually associated with the third transition stage. However, the mass increased more dramatically and at earlier times than for previously published mass gain curves. It was also noticed that the samples were heavily oxidized along their edges. This heavy oxidation caused the edges to curl up, possibly allowing runaway oxidation. This phenomenon has been noted by Madeyski et al, on thin Zr samples (26). The edge curl effect explains the rapid change in the rate of mass gain. During the curve fitting with the model, the section of the curve assumed to be associated with the edge curl effect was neglected during the curve matching procedure.

Isothermal Model Correlations with Oxide Thickness Measurements

The same samples for which mass gain results correlated were also employed for oxide thickness measurements. Edge views of the oxidized samples were enlarged 200 times by SEM. A typical view is shown in Figure 17 which is an SEM enlargement of sample Zr34. The surface oxide layer is fairly even, with no spots of local heavy oxidation evident. Only a small representative portion of the sample was photographed. The thickness of the surface oxide was determined by measuring several points on the picture, from which an average thickness was determined. This method of measurement is accurate to $\pm 5 \times 10^{-6}$ cm. Hence, the largest error involved may result from the degree of resemblance of



50 microns

Figure 17. SEM 200X enlargement of polished Zr edge showing surface oxide growth after 6.3 hours at 1173 K in medical grade O_2 .

the measured edge to that of the entire sample. Visual inspection in the SEM indicated that the samples were fairly uniform.

Evaluation of $D_{\sigma}\delta C_{\sigma}$ from Experimental Oxide Thicknesses. The value $D_{\sigma}\delta C_{\sigma}$ was changed in the model until the model's value of oxide thickness at a specific exposure time and temperature matched those measured experimentally. Model predicted oxide thicknesses were adjusted until they matched the experimental values to $\pm 1 \times 10^{-6}$ cm. Table 7 shows the estimated values of $D_{\sigma}\delta C_{\sigma}$ obtained by this method. What is noticed is that for increasing O_2 exposure times at constant temperatures, decreasing values of $D_{\sigma}\delta C_{\sigma}$ were calculated. The largest decrease is 37 % at 1173 K for a 500 % increase in exposure time.

Experimental Errors Involved with Oxide Thicknesses. There are few published oxide thickness measurements at temperatures studied in this work. However, a general comparison can still be made at other temperatures. Experimental oxide layer thicknesses as functions of exposure time are shown in Figure 18, together with published curves. Curves (a), (b) and (d) represent this work's observations at 1243, 1173 and 1073 K respectively. Curve (c) is J.P. Pemsler's at 1373 K (34) and curve (d) is the results from C.J. Rosa at 1123 K (33). The curves all have the same general shape, but the surface oxides produced during this research are thicker than those reported by

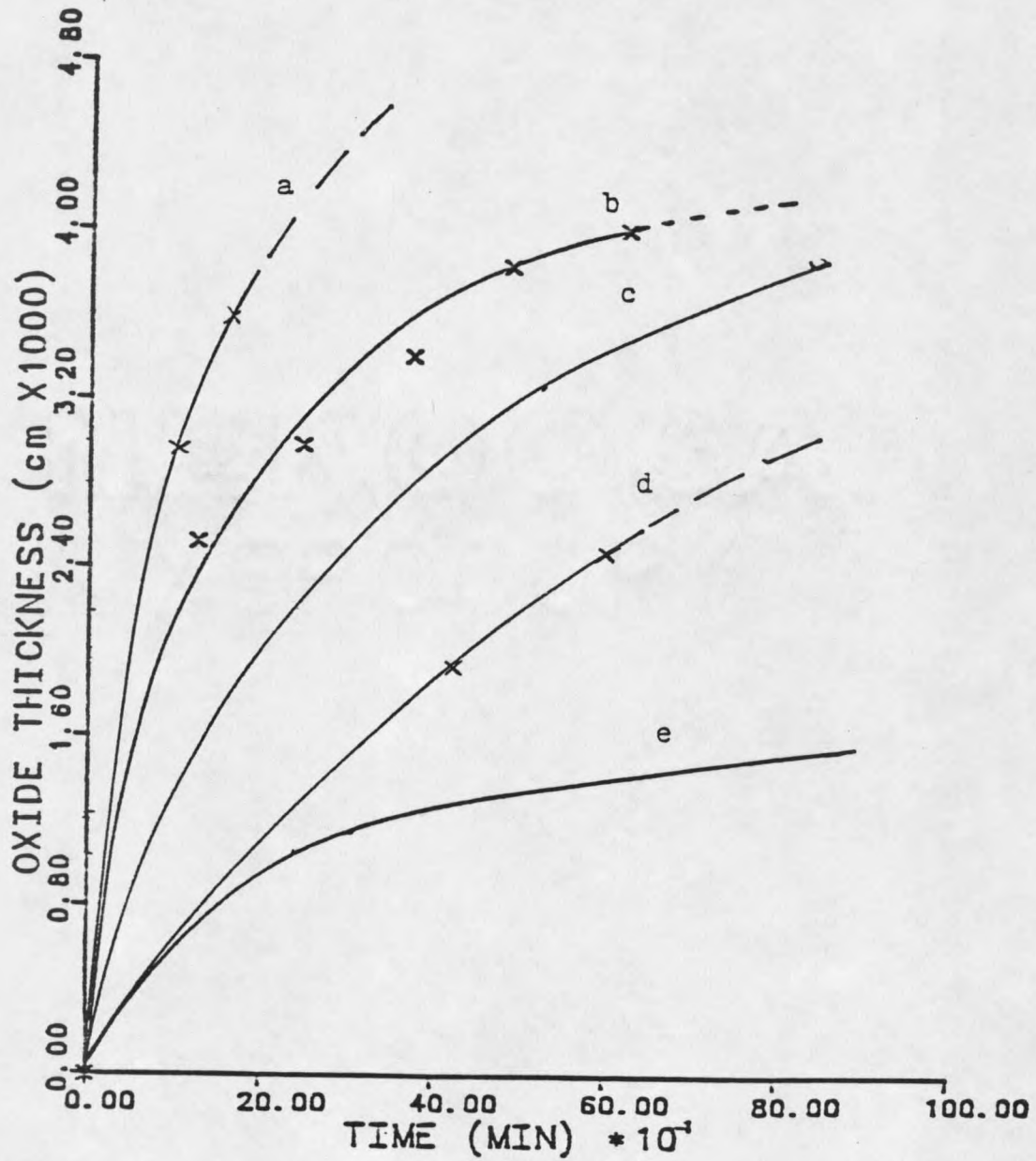


Figure 18. Experimental and published oxide thicknesses:
 (a) this research at 1243 K, (b) this research at 1173 K, (c) Pemsler at 1373 K (34),
 (d) this research at 1073 K, (e) Rosa at 1123 K (33).

Pemsler and Rosa when compared to similar temperatures and times. The larger oxide thicknesses obtained here are possibly due to the thin samples used in this research. Since the samples are so thin, 0.025 cm, the oxygen concentration gradient in the bulk Zr decreases due to diffusion of O into the bulk. This would result in slowing the transport of oxygen into the bulk. Hence, more oxygen will react to form ZrO_2 with a corresponding thicker oxide layer when compared to surface oxides grown on thicker bulk Zr samples. The samples used by Rosa were 0.35 cm thick. The reproducibility of oxide thickness data at a specific O_2 exposure time and temperature was not determined.

Since the oxide thickness of the samples could be measured accurately, it was possible to obtain $D_{\text{O}}\delta C_{\text{O}}$ values that were sensitive to $\pm 1 \times 10^{-6}$ mole O/cm sec. However, due to the inability to obtain isothermal conditions because of warm up and cool down effects, the values of $D_{\text{O}}\delta C_{\text{O}}$ may not exhibit that tolerance. To determine the accuracy of these results, a non-isothermal section was added to the model, and will be discussed later.

Determination of D_{O} as a Function of Temperature

Since there is very little literature reporting $D_{\text{O}}\delta C_{\text{O}}$ values, it was decided to evaluate D_{O} as a function of temperature. To evaluate D_{O} a literature value for δC_{O} was used. Values for δC_{O} have been determined by several

researchers (35,36,37). For this research the value of δC_{σ} given by Pawel was used (36). The value is a function of temperature and is written:

$$\delta C_{\sigma} = C_{\sigma\alpha} - C_{\sigma\beta} \quad (13)$$

where:

$$C_{\sigma\alpha} = 0.09481 - 4.6875 \times 10^{-6} \times T \quad \text{g mole O/cc}$$

$$C_{\sigma\beta} = 0.09444 \quad \text{g mole O/cc}$$

T = Temperature in K

Table 8 shows the resulting values of D_{σ} calculated at each temperature by both the mass gain and the oxide thickness measurements.

Since D_{σ} was determined at three temperatures, it is possible to correlate D_{σ} with temperature. This is accomplished by plotting $\ln D_{\sigma}$ vs $1/T$. The intercept is D_0 , and the slope is Energy of activation, E. This plot is presented in Figure 19 along with several published correlations. The values of D_{σ} as a function of temperature obtained for both the curve fitting method and the oxide thickness matching method are:

Mass Gain Curve Fitting; $D_{\sigma} = 1.58 \times 10^{-5} \text{EXP}(-20700/R T)$

Oxide Thickness Matching; $D_{\sigma} = 2.00 \times 10^{-2} \text{EXP}(-34300/R T)$

Where R is the ideal gas constant 1.987 cal/mole K, and T is temperature in K.

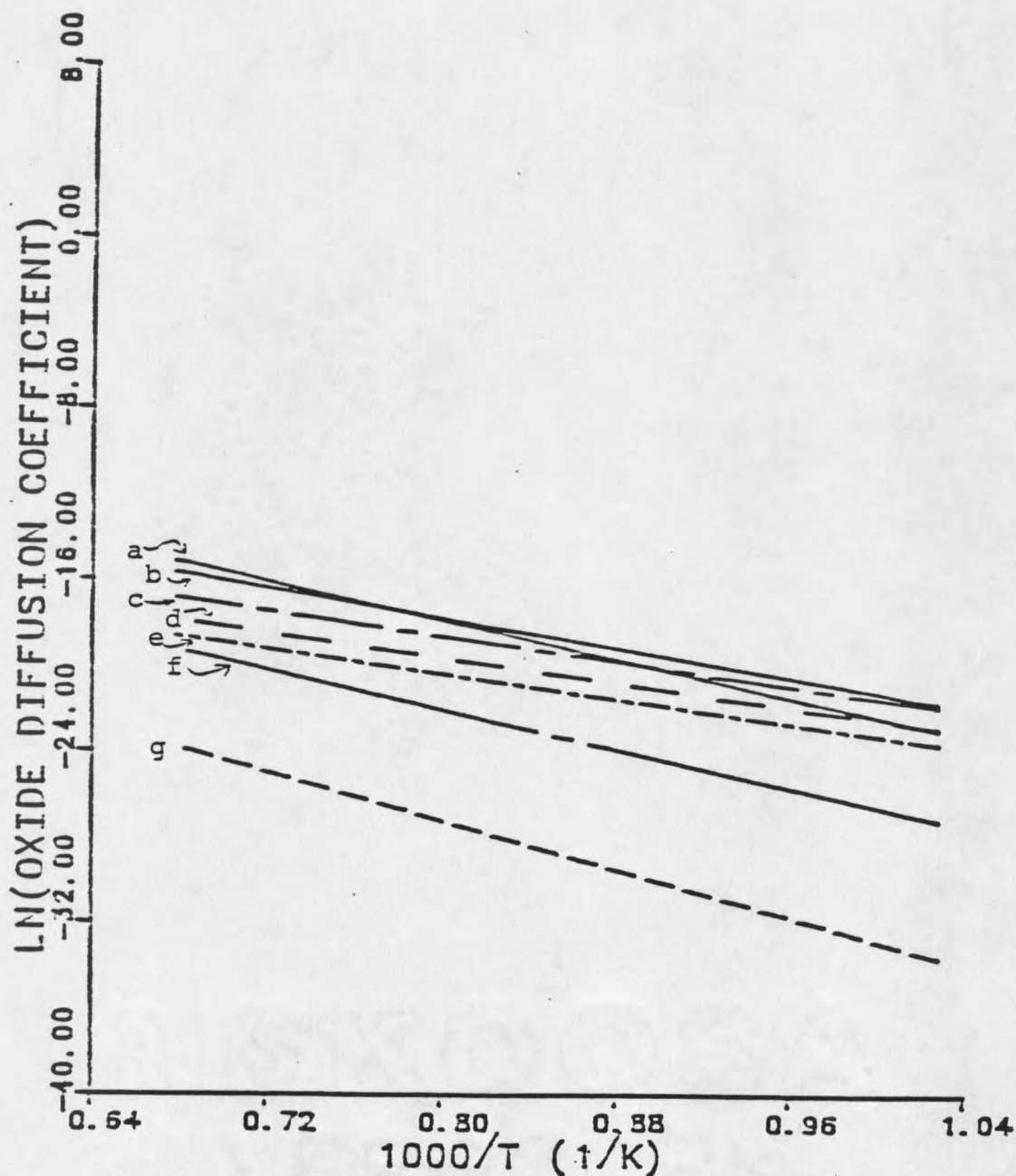


Figure 19. Various diffusion coefficients of O^{2-} in ZrO_2 :
 (a) this research from mass gain curve fitting;
 (b) this research from oxide thickness measurements; (c) and (d) Rosa and Hagel below and above the transition temperature respectively (38); (e) Smith (39); (f) Keneshea and Douglass (15); (g) Madyski and Smeltzer for single crystal near stoichiometric ZrO_2 (26).

Table 8. D_{σ} from oxide thickness measurements and mass gain curve fitting.

Run #	Time Hours	Temp. K	δC_{σ} mole O/cc X 1000	D_{σ} From Oxide Thickness cm ² /sec	D_{σ} From Curve Fit cm ² /sec
Zr38	6.9	1073	-4.66	2.19X10 ⁻⁹	9.72X10 ⁻¹⁰
Zr39	10.0	1073	-4.66		
Zr37	2.1	1173	-5.13	9.96X10 ⁻⁹	2.22X10 ⁻⁹
Zr36	4.1	1173	-5.13	7.66X10 ⁻⁹	
Zr34	6.3	1173	-5.13	6.80X10 ⁻⁹	
Zr35	8.2	1173	-5.13	6.57X10 ⁻⁹	
Zr33	10.4	1173	-5.13	5.71X10 ⁻⁹	
Zr40	1.8	1243	-5.46	2.09X10 ⁻⁸	2.00X10 ⁻⁸
Zr41	2.7	1243	-5.46	2.01X10 ⁻⁸	

Deviations Between Experimental and Published Values of D_{σ} . Several published correlations of D_{σ} are shown in Figure 19, along with the results obtained here. Curves (a) and (b) are from this work by mass gain curve fitting and oxide thickness matching, respectively. The slope between the correlations found by the two experimental methods of mass gain curve fitting and oxide thickness matching are not equal, as can be seen in Figure 19. The deviations between the two methods range from about 0.0 percent at 1243 K to about 2 orders of magnitude 1073 K. However, the deviations between the two experimental results are not very significant when compared to the deviations found in published results. There are several orders of magnitude variation between various published correlations. The values determined by Hagel and Rosa are close to the values found

in this research (38). Hagel and Rosa used a mathematical model and mass gains to evaluate D_o . There are five orders of magnitude difference between this research and the value reported by A. Madeyski et al. (26). Madeyski used O_{18} gaseous exchange with near stoichiometric single crystal ZrO_2 . The value of D_o obtained by Smith is also reasonably close to those from this work (39). Smith determined D_o by obtaining mass vs. time data at a relatively low temperature of 659 K and assuming that diffusion of oxygen into bulk Zr was negligible. Curve (f) in Figure 19 was developed by Keneshea and Douglass (15). Their correlation is not in good agreement with this work. It was obtained by use of O_{18} gaseous exchange with microspheres of ZrO_2 , and is assumed by Keneshea and Douglas to be primarily related to lattice diffusion.

The possible effect of changes in δC_o values is not large enough to change D_o by an order of magnitude. Also, there is not an order of magnitude deviation of D_o within the experimental results of this work. Hence, another explanation for the large difference between this work's results and those found in the literature must exist. The most probable explanation is that the oxide characteristics are changing during the time of oxidation. The surface oxide's physical characteristics are believed to be changing for two reasons. One is the fact that D_o values obtained on surface oxides grown on bulk Zr are larger by several orders

of magnitude than D_{σ} values obtained in specially prepared bulk ZrO_2 samples. The second is the decrease in D_{σ} with an increase in length of oxygen exposure at a constant temperature.

Changing Characteristics of the Oxide. Changing characteristics of the oxide would result in a change in the ratio of grain boundary diffusion to lattice diffusion as the oxidation process proceeds. Since there is some transport through the grain boundaries and some through the lattice, D_{σ} determined by the model is actually $D_{\sigma eff}$. Which can be written as: (26)

$$D_{\sigma eff} = D_L(1-f) + D_B f \quad (14)$$

Where:

D_L - Lattice diffusion coefficient

D_B - Boundary diffusion coefficient

f - Fraction of the total available oxygen sites lying at the crystallite boundaries.

It is calculated that f is approximately 0.1 if a crystallite is considered to be 10 Angstroms in width (26).

At 1173 K, $D_{\sigma eff} = 7.98 \times 10^{-9}$ cm²/sec, from oxide thickness measurements. For near stoichiometric single crystal zirconia $D_L = 5 \times 10^{-13}$ cm²/sec, found by Madeyski (26). Using equation 14 it is found $D_B = 7.98 \times 10^{-8}$ cm²/sec. This indicates that the primary diffusion path of O^{2-} in the surface oxides developed in this work is boundary diffusion. The ratio of $D_B/D_L = 1.6 \times 10^5$, is larger than others reported by Douglas

which were about $D_B/D_L \sim 10^4$ (2). It is not surprising that D_B/D_L is larger, since this research deals with the initial stages of oxidation at which time the oxide crystallites in the surface oxide are small. Hence, more grain boundary area and more transport along the boundaries. However, the crystallites start out small and increase in size as the oxide grows. Therefore, the fraction of total available oxygen sites lying on the crystallite boundaries, f , changes with time as oxidation proceeds.

Since the oxide characteristics are changing during the time of oxidation then D_G will also change. This probably explains why a different value of D_G is found for different lengths of runs at the same temperatures as can be seen in Table 8. The values of D_G decrease with an increase in oxidation time. This corresponds well with the fact that the crystallites start out small and increase in size with time of oxidation. The amount of area available for boundary diffusion decreases as the crystallite size increases. To produce an accurate model D_G must be expressed as a function of time or extent of oxidation. This can be accomplished by making many experimental runs at varying times at several temperatures. Accurate control of temperature and time would be very important.

Effect of Warm-Up and Cool-Down. A correlation between time and temperature was developed from the experimental system. With this correlation a non-isothermal model was

developed, and is shown in the Appendix as Model II. The correlations for D_o derived from the isothermal model were then used in the non-isothermal model. The values of oxide thickness evaluated from the non-isothermal model are compared to measured thicknesses in Table 9. The largest deviation between experimental and model oxide thickness at each temperature is -5.9, -25.2 and 12.4 at 1073, 1173 and 1243 K respectively. A comparison of total mass gain curves between both the non-isothermal and isothermal models with experimental at 1073 K is shown in Figure 20. There is very little difference between the isothermal and non-isothermal curves, less than the estimated experimental error of $\pm .7$ mg/cm². Hence, less error occurs with assuming isothermal conditions than occurs from other sources. The other temperatures of 1173 and 1243 K have similar results.

Table 9. Experimental oxide thicknesses and the percent deviation vs. predicted non-isothermal model, oxide thicknesses.

Run #	Time Hours	Temp. K	Experimental Oxide Thickness X 1000 cm	Non- isothermal Oxide Thicknesses X 1000 cm	% Deviation
Zr38	6.9	1073	1.930	2.044	-5.90
Zr39	10.0	1073	2.585	2.464	4.68
Zr37	2.1	1173	2.525	2.160	14.45
Zr36	4.1	1173	2.985	3.038	-17.76
Zr34	6.3	1173	3.410	3.775	-10.70
Zr35	8.2	1173	3.840	4.367	-3.72
Zr33	10.4	1173	4.015	5.025	-25.15
Zr40	1.8	1243	3.338	2.924	12.40
Zr4	12.7	1243	3.995	3.627	-9.21

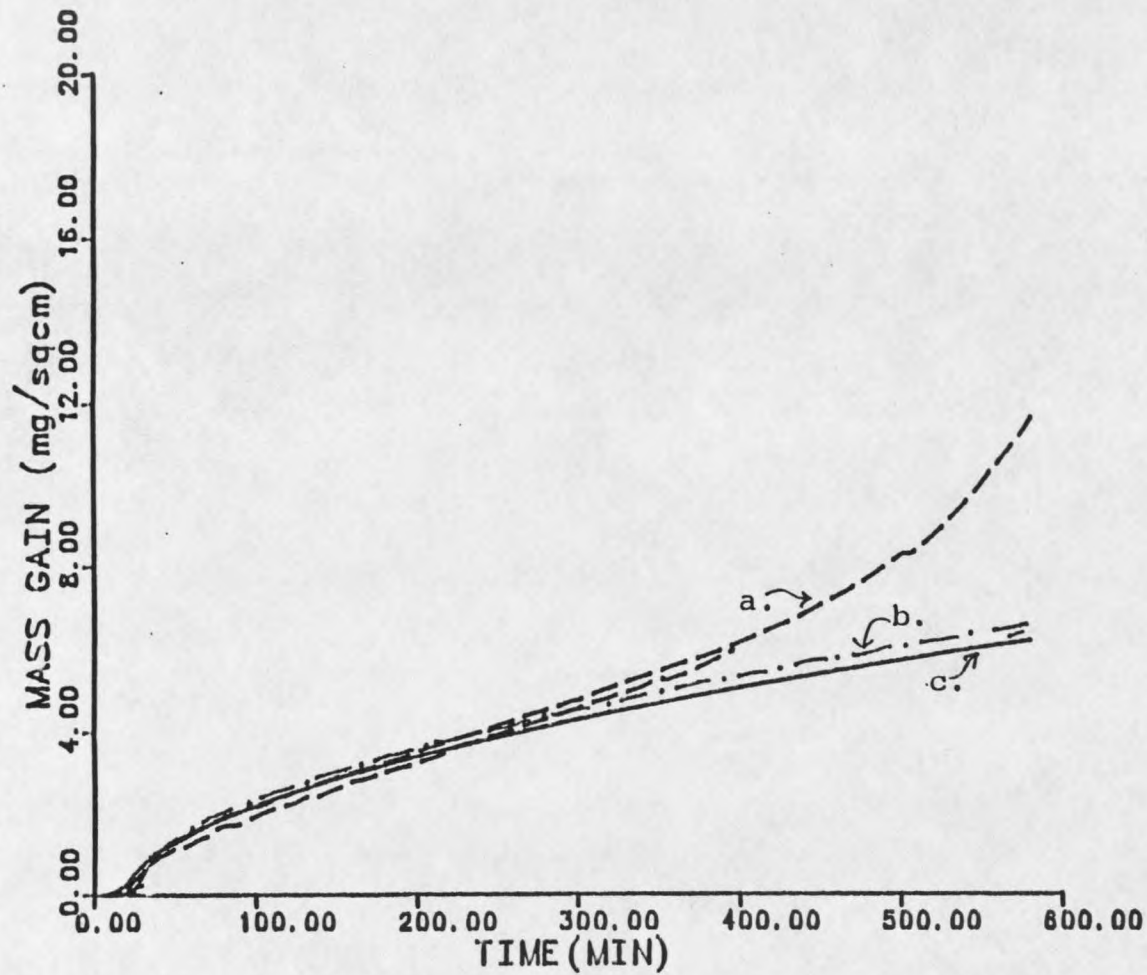


Figure 20. Experimental and theoretical mass gains at 1073 K.
 a. Experimental b. Isothermal model c. Non-isothermal model.

